Basal icequakes recorded beneath an Alpine glacier (Glacier d 'Argentiere, MontBlanc, France): evidence for stick-slip motion

Agnès Helmstetter, Barbara Nicolas, Pierre Comon, Michel Gay

Basal icequakes recorded beneath an Alpine glacier (Glacier d'Argentière, Mont Blanc, France): evidence for stick-slip motion?

Agnès Helmstetter[1], Barbara Nicolas[2], Pierre Comon[2] and Michel Gay[2]
[1] University of Grenoble, CNRS, ISTerre, F-38000 Grenoble, France.
[2] Grenoble INP, GIPSA-Lab, CNRS, Grenoble, France.

Abstract

While basal icequakes associated with glacier motion have been detected under Antarctica for several decades, there remains very little evidence of stick-slip motion for Alpine glaciers. Here we analyzed 2357 basal icequakes that were recorded at Glacier d'Argentière (Mont-Blanc Massif) between February and November of 2012, and that are likely to be associated with basal sliding. These events have been classified into 18 multiplets, based on their waveforms. The strong similarity of the waveforms within each multiplet suggests an isolated repeating source. Despite this similarity, the peak amplitude within each multiplet varies gradually in time, by up to a factor of 18. The distribution of these events in time is relatively complex. For long time scales we observe progressive variations in the amplitudes of events within each multiplet. For intermediate time scales (hours), the events occur regularly in time, with typical return times of several minutes up to several hours. For short time scales (from 0.01 to 100 s), the largest multiplet shows clustering in time, with a power-law distribution of the interevent times. The location of these events and their focal mechanisms are not well constrained, because most of these events were detected by a single seismometer. Nevertheless, the locations can be estimated with an accuracy of a few tens of meters using a polarization analysis. The estimated average depth of the basal events is 179 m, which is in good agreement with the estimated glacier thickness. The relative changes in distance between the source and the sensor can be measured accurately by correlating separately the P-wave and S-wave parts of the seismograms of each event with the template waveforms, which are obtained by averaging the signals within each multiplet. We observed small variations in the times between the P-wave and the S-wave of up to 0.6 ms over 50 days. These variations cannot be explained by displacement of the sensor with respect to the glacier, but might be due to small changes in the seismic wave velocities with time. Finally, we found using numerical simulations that the observed signals are better explained by a horizontal shear fault with slip parallel to the glacier flow, than by a tensile fault. These results suggest that the basal events are associated with stick-slip motion of the glacier over rough bedrock. The rupture length and the slip are difficult to estimate. Nonetheless, the rupture length is likely to be of the order of meters, and the total seismic slip accumulated over one day might be as large as the glacier motion during the most active bursts.

1 Introduction

Glaciers and ice-streams in Antarctica are known to show stick-slip behavior [*Anandakrishnan and Bentley*(1993), *Anandakrishnan and Alley*(1994), *Bindschadler et al.*(2003), *Danesi et al.*(2012)]. Slip events at the ice-bedrock interface show broad diversity of size, with rupture lengths varying from a few meters [*Smith*(2006)] to several hundred kilometers [*Wiens et al.*(2008)]. These events generally have quasi-periodic behavior [*Smith*(2006), *Wiens et al.*(2008), *Zoet et al.*(2012)]. The average interevent time varies across several orders of magnitude, with a range from a few minutes [*Smith*(2006), *Zoet et al.*(2012)] to half a day [*Wiens et al.*(2008)].

Basal processes are inherently difficult to study because of access issues. Therefore, remote methods, such as seismology, can be useful to gain insight into glacial processes. Basal seismicity may provide information about the subglacial conditions, such as the bedrock properties [*Smith*(2006)], stress distribution [*Anandakrishnan and Bentley*(1993)], subglacial water flow [*Winberry et al.*(2009)], and basal fractures [*Walter et al.*(2010), *Walter et al.*(2013)].

While basal icequakes associated with glacier motion are frequent in Antarctica, there is very little convincing evidence of basal icequakes for Alpine glaciers. In many cases, the location and/or the focal mechanisms of these icequakes are not well constrained and it is not clear whether the source of these events is basal slip of the glacier [*VanWormer and Berg*(1973), *Weaver and Malone*(1979), *Deichmann et al.*(2000), *Stuart et al.*(2005), *Caplan-Auerbach and Huggel*(2007), *Roux et al.*(2008), *Christianson*(2012), *Thelen et al.*(2013), *Allstadt and Malone*(2014)]. Moreover, several studies that have attempted to detect basal icequakes in Alpine glaciers did not detect any basal events [*Pomeroy et al.*(2013), *Moore, et al.*(2003)]. Friction experiments with ice samples at the pressure melting point have shown only stable sliding, while stick-slip behavior was observed only for subfreezing conditions [*Zoet et al.*(2013)]. As many mountain glaciers are temperate, these experiments might explain why stick-slip behavior is rarely observed for Alpine glaciers. Basal icequakes have been detected beneath Gornergletscher (Gorner Glacier) and Triftgletscher (Trift Glacier) in Switzerland [*Walter et al.*(2008), *Walter et al.*(2010), *Walter et al.*(2013), *Dalban Canassy et al.*(2013)]. For these studies, moment tensor inversions have suggested that these events are mainly due to the opening and closing of tensile faults within the glacier, in response to changes in subglacial water pressure, rather than to slip events. Icequakes have also been recorded at the base of Engabreen Glacier, a temperate outlet glacier in Norway [*Christianson*(2012)], and at Mount Rainier in the USA [*Thelen et al.*(2013), *Allstadt and Malone*(2014)]. These three studies detected quasi-periodic events with typical interevent times of 2 min to 40 min, and magnitudes between -1 and 0. Although these events could not be located precisely, their quasi-periodic behavior and the similarity of the waveforms within each multiplet suggest that these icequakes are produced by stick-slip motion at or near the ice-bedrock interface [*Christianson*(2012), *Thelen et al.*(2013), *Allstadt and Malone*(2014)].

In a few cases, subglacial processes can be observed directly, due to the presence of tunnels underneath the glaciers [*Vivian and Bocquet*(1973), *Goodman et al.*(1979), *Fischer and Clarke*(1997), *Moore, et al.*(2003)]. [*Goodman et al.*(1979)] recorded strain variations in a tunnel a few meters beneath Glacier d'Argentière. However, strain offsets can be explained by both rupture of frozen patches of ice at the ice-bedrock interface and the opening of cracks. [*Fischer and Clarke*(1997)] used a "drag-spool" to measure basal sliding underneath Trapridge Glacier, Yukon Territory, Canada. They observed an increase in sliding rate slip events that occurred every day when there was increased water pressure.

As well as stick-slip events, Alpine glaciers also show variations of the flow rate over longer timescales, known as "speed-up events" [*Iken et al.*(1983), *Fischer and Clarke*(1997),

Anderson et al.(2004), *Sugiyama and Gudmundsson*(2004), *Ponton et al.*(2014)]. These events occur in the melt season, when the basal water pressure increases, and they can last for several hours or several weeks.

Glacier flow and tectonic fault zones share several properties. Slip occurs as a result of tectonic loading for earthquakes and of glacier flow for icequakes. The motions of glaciers and faults show fluctuations at very different time scales, from rapid slip events due to dynamic frictional instabilities (i.e., icequakes or earthquakes) at time scales of the order of 1 s, up to smooth "speed-up" or "slow-slip" events [*Ide et al.*(2007)] at times scales of hours or days. The sliding motion is also very heterogeneous in space. Both glaciers and tectonic faults show "asperities" [*Vidale et al.*(1994), *Nadeau, et al.*(1995)], or "sticky spots" [*Anandakrishnan and Alley*(1994)], which are characterized by repeating stick-slip events, and are surrounded by sliding or creeping zones. Analyzing basal icequakes might thus be helpful to better understand repeating earthquakes, because a glacier is a relatively simple environment. Glaciers allow direct access to the rupture plane and show much faster displacements than tectonic faults, with many more slip events produced over several weeks than can be detected for tectonic faults over several decades.

[*Zoet et al.*(2013)] suggested that stick-slip behavior can be promoted by high levels of rock debris inside ice that is moving over rough bedrock, by sub-freezing temperatures, by low basal water pressure, and/or by fast flow and high basal shear stress. Basal icequakes are also more frequent in the absence of a till layer at the base of the glacier [*Anandakrishnan and Bentley*(1993), *Smith*(2006)]. Several external forces can also influence or trigger basal icequakes, such as oceanic tidal oscillations [*Bindschadler et al.*(2003)], additional weight due to snow falls [*Allstadt and Malone*(2014)], and distant earthquakes [*Walter et al.*(2014)].

Apart from basal slip, other sources of seismic signals produced by glaciers include crevassing [*Neave and Savage*(1970)], resonance in subglacial water-filled cracks and conduits [*Métaxian, et al.*(2003)], and calving events [*O'Neel et al.*(2007), *Nettles and Ekstrom*(2010)]. These events usually constitute the main sources of seismic events detected for glaciers. Seismic events have also been detected at intermediate depths, as below the depth of open crevasses but above the ice-bedrock interface [*Deichmann et al.*(2000), *Walter et al.*(2009), *Helmstetter et al.*(2014)]; these might be due to hydraulic fracturing.

In this study, we have analyzed seismic signals of basal icequakes that were detected at Glacier d'Argentière (Mont-Blanc massif) in 2012. In addition to seismic signals that appear to be associated with shallow sources, such as serac falls or crevassing, we identified two classes of deep icequakes. The first class of deep events corresponds to icequakes of intermediate depth, located at 70 m meters above the bedrock. These events are described in a companion paper [*Helmstetter et al.*(2014)]. This paper is focused on the second class of deep icequakes, which were located at or near the ice-bedrock interface, and therefore these are referred to as "basal icequakes". We describe the distribution of these events in time, space and magnitude, and we discuss the possible mechanisms responsible for these events.

2 The study area

Glacier d'Argentière is a temperate, hard-bedded glacier that is located in the Mont Blanc massif, in the French Alps. Glacier d'Argentière has a length of about 10 km, from its top part at an altitude of 3400 m asl, to its tongue at an altitude of 1600 m asl. In 2003, this glacier covered a surface area of 12.4 km^2 [*Vincent et al.*(2009)]. Numerous glaciological measurements (e.g., mass balance, thickness variations, ice-flow velocity, and length fluctuations) have been carried out on Glacier d'Argentière since

the beginning of the twentieth century [*Hantz*(1981), *Vincent et al.*(2009)]. These data are available from the GLACIOCLIM database (`www-lgge.obs.ujf-grenoble.fr/ServiceObs`). Similar to many Alpine glaciers, Glacier d'Argentière reached its maximum velocity and thickness in the early 1980s, which was then followed by a sharp decrease over the next three decades.

Our seismic network was installed on Glacier d'Argentière at an elevation of 2400 m asl (see Figure 1). At this location, the ice-flow velocity decreased from 140 m/yr to 81 m/yr between 1985 and 2007 [*Vincent et al.*(2009)]. During this time, the thickness also decreased by 23 m, and the glacier length decreased by 550 m. Before 2000, the surface ice-flow velocities were measured each year in September, from stake displacements. More recently, the flow velocities have been measured yearly using GPS. Continuous GPS measurements started in 2007 [*Ponton et al.*(2014)]. When the displacement velocity of station SERA, which is located near to our seismic network (see Figure 1a), is averaged over 2-day periods, it varies from 0.17 m/d in winter to 0.21 m/d in summer. The bedrock topography along several profiles has been determined using seismic soundings, and several boreholes were drilled to check these data [*Hantz*(1981)]. The average uncertainty of the bedrock topography is of the order of 10 m, although sometimes this can exceed 30 m [*Hantz*(1981)].

The profile located 200 m upstream from our seismic sensor has a maximum ice thickness of 219 m. This thickness can be decreased by 17 m to account for the glacier thinning between 2003 and 2012 (C. Vincent, personal communication, 2014), which gives a maximum thickness of 202 m for 2012. The glacier has an icefall in its lower part, between 2000 m asl and 2300 m asl, at Lognan, where the bedrock is now apparent over the full width of the glacier. Behind the icefall, a network of industrial cavities and galleries was dug into the bedrock at about 5 m under the glacier bed, by Emosson S.A. (a hydroelectric power company), at 2170 m asl.

3 Instrumentation

In the present study, we analyze seismic events recorded in 2012 using two different seismic networks, as shown in Figure 1. Most seismic events were detected by a single three-component accelerometer (S_0), which was in operation during five time windows that covered 44 days, between February and June of 2012: February 17-25, March 12-17, March 30 to April 12, April 25 to May 3, and June 5-19. The gaps in the monitoring were due to the numerous difficulties associated with seismic monitoring on glaciers, such as: insufficient power supply, insufficient space on the memory card, and difficult access to the glacier. The accelerometer was a MEMS-based Sercel DSU3, which recorded in continuous mode at a sampling rate of 1000 Hz. It was located in the center of the glacier at an elevation of 2380 m asl, about 600 m upstream of the Lognan icefall. The sensor was installed in winter by digging several meters into the snow, down to the snow-ice interface. When the sensor was retrieved on 19 June, all of the snow had melted and the sensor was recovered lying on the ground. On May 9, there was still 2.5 m of snow above the sensor, and we checked that the orientation of the sensor had not changed. For the last acquisition period (June 5-19), the data were very noisy, as the sensor was close to the surface, or lying on the ground.

We performed another acquisition from 17 to 30 November 2012, using two types of sensors. Two DSU3 accelerometers (named as S_1 and S_2) were installed about 100 m downstream of the location of sensor S_0. In addition, we installed one seismic antenna (station ABC) with nine one-component 2 Hz velocimeters aligned in a direction perpendicular to the glacier flow, with an interdistance of 10 m. All of the stations were recording in continuous mode at a sampling rate of 1000 Hz.

Meteorological data were obtained from two stations. One station was available from GLACIO-

CLIM, and it was installed outside the glacier, at about 600 m from sensor S_0; this station measured temperature and solar radiation. The other station that belonged to Météo-France was installed 4 km north of the network, at an elevation of 1500 m asl; this station provided precipitation data.

4 Detection and classification of seismic events

We first applied a detection algorithm [*Helmstetter and Garambois*(2010)] to the continuous seismic data, to identify seismic events. By looking at the seismograms of the detected events, we identified some repeating events with similar waveforms, short durations (about 0.1 s), high frequencies (about 100 Hz), impulsive first arrivals, distinct P-waves and S-waves, and no surface waves. These characteristics are similar to seismic signals of deep icequakes described in previous studies on Alpine glaciers [*Deichmann et al.*(2000), *Walter et al.*(2008), *Walter et al.*(2010), *Walter et al.*(2013), *Dalban Canassy et al.*(2013)].

We chose one of these signals as a template event and performed cross-correlation of this template signal with the full continuous database, to detect all similar events belonging to the same "multiplet". We first computed the normalized cross-correlations for each channel, and then the average correlations over the three components. We considered a correlation peak as potential detection if the correlation exceeded 0.5. Similar methods have frequently been used to detect icequakes [*Carmichael et al.*(2012), *Mikesell et al.*(2012), *Thelen et al.*(2013), *Allstadt and Malone*(2014)]. We then visually inspected all of these events, and rejected those that were significantly different from the template event. We checked that the main characteristics of the signals were similar to those of the template: high frequency P-waves, lower-frequency S-waves, presence of both positive and negative pulses, and the timing and relative amplitudes of the first arrivals for the P-waves and S-waves.

Most incorrect detections were due to spikes or were associated with shallow or intermediate depth events, with a time delay between the P-waves and S-waves that was much shorter than for the template signal. Some of the signals had similar characteristics to the template (e.g., same frequency content, distinct P-waves and S-waves) but showed different waveforms. These events were classified as a new multiplet, and were used as templates to detect similar events. The fraction of false detections was very small for templates with impulsive P-waves and S-waves. But for a few templates with very weak S-waves, or when the correlation threshold was decreased to 0.4, we found many more false detections than true basal icequakes.

After the manual selection of the signals, we defined a new template signal as the average of the waveforms (stack) for all of the events within each multiplet. Before averaging, the signals were normalized according to the maximum amplitude of the signal. The peak amplitude of each event was given by multiplying the peak amplitude of the template signal by the "scaling factor" [*Gibbons and Ringdal*(2006)], which was defined by the unnormalized cross correlation coefficient divided by the inner product of the template waveform. The updated template signal was again correlated with the continuous data, with manual checking all of the signals. The average correlation between each event of a multiplet and the template signal was 0.79. Lower correlations generally corresponded to low-amplitude events or to spikes on the seismograms, especially for the east/west component, which was very noisy. Some signals also had low correlations because several events overlapped with a time delay of several hundredths of a second.

We identified 18 multiplets of basal icequakes, the waveforms for which are shown in Figure 2. The multiplets are labelled as *A*-*R* in chronological order. The remarkable similarity of the waveforms within each multiplet suggests that they share the same source location and source mechanism. As

cluster M was active continuously for June 5-18 with no apparent change in seismic waveforms, this suggests that the orientation of the sensor remained correct during this time period.

For most multiplets, the signal onset shows high-frequency oscillations. We suspect that this pattern is an artifact due to aliasing effects, although the recording station includes an anti-aliasing filter. Figure 3 shows the spectral density for a basal icequake of multiplet B. Most of the P-wave energy is between 200 Hz and 450 Hz, so it is close to the Nyquist frequency (500 Hz). In future experiments, the sampling rate should be increased to avoid aliasing effects. Because of this artifact, it is difficult to precisely determine the arrival times of the P-waves, and their polarity. Figure 3 also highlights the different frequency contents for P-waves and S-waves. The main frequency of the S-waves was $\approx$ 70 Hz, so there is no problem of aliasing.

In terms of their duration and frequency content, the waveforms of the basal events shown in Figure 2 are very similar to those detected at Gornergletscher and Triftgletscher in Switzerland [*Walter et al.*(2008), *Walter et al.*(2010), *Walter et al.*(2013), *Dalban Canassy et al.*(2013)]. However, the correlation between the waveforms is stronger than for basal icequakes detected in Switzerland. These signals are instead very different from the signals detected at Mount Rainier [*Thelen et al.*(2013), *Allstadt and Malone*(2014)], which had a much lower frequency content, of 1 Hz to 6 Hz, and much longer durations, of about 20 s, despite the relatively small magnitudes of between -1 and 0. [*Thelen et al.*(2013)] suggested that the low frequency content of these signals can be explained by path effects. Indeed, all of the stations that detected these icequakes were installed on rock several kilometers from the source, and a layer of low-velocity volcanic material underlies the glacier.

5 Location of basal icequakes

Only the last multiplet R occurred in November 2012, when station ABC was in operation. For the other multiplets, we can nevertheless obtain rough estimations of the source locations with a single three-component sensor using polarization analysis. Locating the sources of basal icequakes requires knowledge of the seismic-wave velocities. We assume a uniform seismic-wave velocity of 3600 m/s for the P-waves, and 1610 m/s for the S-waves. These values were measured by [*Vallon*(1967)] for Glacier du Tacul, a temperate glacier in the Mont-Blanc massif, which is at about the same altitude as the present seismic network. These velocities are a little slower than those of V_P = 3630 m/s and V_S = 1790 m/s reported by [*Walter et al.*(2010)] for Gornergletscher, a glacier in Switzerland that contains some cold ice with larger seismic-wave velocities than for temperate ice. For events located further than a few hundred meters from the sensor, the first arrivals might be the refracted waves. In this case, computing the travel-times requires additional information on the seismic-wave velocities in the bedrock, and on the bedrock topography. We assumed that the seismic-wave velocities in the granitic bedrock were 5000 m/s for P-waves, and 2550 m/s for S-waves [*Walter et al.*(2010)]. As seismic wave velocities are faster in the bedrock than in the ice, refracted waves can propagate at the ice-bedrock interface. These waves have an incidence angle that is the same as the critical refraction angle given by $\phi_r = \sin^{-1}(3610/5000) = 46$ degrees.

For multiplet R, we located the source by manually picking the first P-wave and S-wave arrivals at 11 sensors (i.e., station ABC and accelerometers S_1 and S_2). We searched for the location that minimized the travel-time residuals, on the assumption that the first arrivals were direct waves. The estimated location is 358 m south-east of sensor S_1 (Figure 4b, red cross). The time residuals are very small, with a root-mean-square error of 0.08 ms. The estimated depth of 182 m is close to the glacier thickness of 196 m, but the uncertainty for the depth was very large. The 95% confidence intervals

were estimated by perturbing the P-wave and S-wave arrival times, assuming Gaussian noise with a standard deviation of 1 ms. The longest axis of the error ellipse had a length of 45 m. The vertical error was 103 m, which was much larger than the horizontal error.

At this distance from the source, the first P-wave arrival should be the refracted wave. We did not attempt to compute travel-times for refracted waves, because the bedrock topography is not well known. Moreover, when using synthetic seismograms generated with an ice-rock interface at 190 m depth (see section 8), we found that the refracted P-wave had a much smaller amplitude than the direct P-wave. It is thus possible that the picked arrival time corresponds to the direct wave. If, on the contrary, we picked the refracted wave, the assumption that this was a direct P-wave would lead to underestimation of the source-sensor distance, and overestimation of the depth. A crude estimation can be obtained by assuming refracted P-waves and S-waves and a horizontal ice layer of 190 m, and then by fixing the source depth at the ice-bedrock interface. This yields an estimated source-sensor distance of 402 m, compared with 358 m when assuming direct waves. For all of the other multiplets, the incidence angle was smaller than for multiplet R, and therefore the location error due to refracted waves should be less important.

For all of the multiplets, we estimated the location of the source with only one 3-component sensor using polarization analysis. First, the distance d between the source and the sensor can be estimated from the time $t_S - t_P$ between the P-waves and S-waves, assuming direct waves

$$d = \frac{t_S - t_P}{1/V_S - 1/V_P} \ . \tag{1}$$

In addition to the distance d, we can also estimate the direction of the source, by analyzing the polarization of the particle motion using the method of [*Vidale*(1986)]. We selected the time window associated with P-waves, from the picked arrival time t_P until $t_P + 0.007$ s. We then applied a singular value decomposition to the analytic signal, without integration or filtering. The azimuth α of the source and the apparent incidence angle ϕ (apparent angle of the ray relative to the vertical axis) were estimated from the direction of the first eigenvector. An example of the waveforms and particle motion for a basal icequake of multiplet R is shown in Figure 5. The apparent angle of incidence of the P-waves is however different from the direction of propagation, because it was affected by reflections at the free surface. We thus used the method of [*Neuberg and Pointer*(2000)] to correct for this effect. Assuming a flat free surface, the true angle of incidence ϕ_c can be estimated from the apparent angle ϕ by:

$$\phi_c = \sin^{-1}\left(\frac{V_P}{V_S}\sin\frac{\phi}{2}\right) \ . \tag{2}$$

Before applying this correction, we subtracted the surface slope along direction α from the apparent incidence angle, as the glacier surface was not horizontal, but had a slope of 8 degrees along the flow direction. The source depth z can then be estimated by $z = d\cos(\phi_c)$. Here, two aspects should be noted. First, Equation (2) has no real solution for $\phi > \phi^*$ with $\phi^* = 2\sin^{-1}\left(\frac{V_S}{V_P}\right) \approx 53$ degrees. Second, for the incidence angles $\phi \approx \phi^*$, small errors in ϕ yield large uncertainties in ϕ_c, and therefore in depth.

The polarization analysis and the correction of Equation (2) were validated with numerical simulations (see section 8). Using synthetic seismograms, the accuracy (i.e., the median of the absolute error) is 4 degrees for the azimuth and 1 degrees for the incidence angle. It is also larger for real signals, due to noise and the heterogeneities of seismic-wave velocities. We can estimate the uncertainty for real events from the variability of the azimuth and incidence angle within each multiplet. Taking all of

the events and averaging over the 18 multiplets, we obtain a standard deviation of 28 degrees for the azimuth and 9 degrees for the incidence angles. The azimuth variability decreases down to 11 degrees for multiplets with an incidence angle $\phi_c > 25$ degrees (1581 out of 2357 events). Small incidence angles correspond to events located almost underneath the sensor. For these events, the azimuth angle is thus very uncertain, but the azimuth error has a much smaller influence on the source location. The location accuracy also depends on the uncertainty of the P-wave and S-wave first arrivals. An error of 3 ms on the arrival time of P-waves or S-waves yields an error of 10 m for the source-sensor distance.

We have also applied the polarization analysis to earthquake signals, to test the method and to check the orientation of the sensors. We selected 16 earthquakes where the distances from the sensor varied from 13 km to 107 km, and the magnitudes from 0.7 to 2.4, which were recorded by station S_0 between February 21 and June 17. We compared the azimuth estimated from the polarization analysis with the azimuth estimated from the earthquake location given by Sismalp (French Alps Seismic Network). The average difference in the azimuth was 0.7 degrees and the standard error was 6 degrees. These data further validate the polarization analysis of real signals, and they suggest that the orientation of sensor S_0 did not change over the duration of the experiment. From 17 to 30 November, we identified three earthquakes recorded by S_1 and S_2 and also present in the Sismalp earthquake catalog, with magnitudes from 1.1 to 3.2, and hypocentral distances from 14 km to 63 km. There was good agreement for S_1 (average difference in the azimuth of 3.7 degrees , and standard error of 7 degrees), but there was a significant bias for S_2 (average difference in the azimuth of 19 degrees , and standard error of 8 degrees). We further estimated the rotation angle between S_1 and S_2 using a selection of 267 seismic events with a cross-correlation between the signals at S_1 and S_2 greater than 0.9. We found a median value for the rotation angle of 16 degrees , with a standard deviation of 12 degrees. These tests suggest that the orientation of sensor S_2 was incorrect, and we thus rotated the horizontal traces by 16 degrees.

Finally, we also applied the polarization analysis to one event of multiplet R, and compared the results with the location estimated by inverting the P-wave and S-wave arrival times (see Figure 4). The locations estimated by the polarization analysis using either S_1 or S_2 are shown by plus signs in Figure 4b.

The error ellipses were obtained by assuming an uncertainty of 1 ms on both the P-wave and S-wave arrival times (standard deviation of a Gaussian distribution). The uncertainty for the azimuth and incidence angles were obtained from the variability among all of the events of multiplet R. For the azimuth angle, the standard deviation was 3.2 degrees for S_1 and 4.8 degrees for S_2. For the apparent incidence angle ϕ, the standard deviation was 3.9 degrees for S_1 and 5.8 degrees for S_2. We computed 1000 locations by perturbing the incidence and azimuth angles and the arrival times. We then estimated error ellipses at the 95% confidence interval. We found that the maximum horizontal distance between the three estimated locations was 46 m, which is within the estimated location error. The estimated depth was 28 m for S_1 and 189 m S_2, but the uncertainty was very large (170 m for S_1 and 269 m for S_2, at the 95% confidence level) because the incidence angles (corrected from the surface slope) are close to ϕ^* ($\phi = 53$ degrees for S_1 and $\phi = 45$ degrees for S_2). In many cases the simulated incidence angle was larger than ϕ^*. In these cases the corrected incidence angle could not be estimated and the depth was fixed to 0.

We then located all of the multiplets by analyzing the polarization of the template signals. The location uncertainties can be obtained from the variability of the azimuth and incidence angles among all of the events of each multiplet. We first assumed that the uncertainty of the azimuth and incidence angle for the stacked signal is given by the standard deviation for all of the events of each multiplet, divided by the square root of the number of events in the multiplet. However, this estimation is likely

to be very optimistic, as it does not account for systematic errors (e.g., undersampling of P-waves, free surface effects, heterogeneity of seismic wave velocities, sensor misorientation). For the largest multiplets, this led to estimated uncertainties that were smaller than the location error obtained from synthetic seismograms. We therefore added 1 degrees to the standard deviation of the incidence angle and 4 degrees to the azimuth angle, using the standard errors measured for the synthetic seismograms. We also assumed a Gaussian error on both the P-wave and S-wave arrival times, with a standard deviation of 1 ms. We then generated a synthetic cloud of points by adding noise to the arrival times and to the azimuth and incidence angles. We computed the horizontal error ellipses at the 95% confidence levels from the covariance matrix, and the vertical error from the 2.5% and 97.5% quantiles of the simulated depths.

Table 1 lists the characteristics of each multiplet, including the depth, incidence and azimuth angles, multiplet duration, and average amplitude. Table 1 also shows the variability of the azimuth and the incidence angles for all of the events of each multiplet. Figure 6 shows the estimated location of all of the basal icequakes. All of the multiplets except F and R have incidence angles smaller than ϕ^*, so we can estimate ϕ_c from Equation (2) and then the depth by $z = d\cos\phi_c$ assuming direct waves. Multiplets F and R have apparent incidence angles greater than ϕ^*, but the difference is within the estimated uncertainty of ϕ. For these multiplets, we could not estimate the depth, so we fixed it to 190 m. Multiplets B and H have corrected incidence angles that are slightly greater than the critical refraction angle $\phi_r = 46$ degrees. For these multiplets, the picked arrival times can correspond to refracted waves, so the distance estimated on the assumption of direct waves might be a little underestimated, and the depth may be inaccurate. Basal events are observed both upstream and downstream from the seismic sensor and up to 358 m away. Excluding multiplets F and R with $\phi > \phi^*$, the depth varies from 129 m to 204 m, with a mean depth of 179 m. The estimated depth is close to the estimated ice thickness along the profile, which is shown as a red line in Figure 6a and is located 150 m downstream from the sensor. The mean difference between the ice thickness and the estimated depth is 2 m. The maximum difference is 33 m for multiplet Q, and this can be explained by the uncertainty for the bedrock topography. By comparing the bedrock topography obtained from seismic sounding with that measured in boreholes, [*Hantz*(1981)] found a mean error of about 10 m, although this sometimes exceeded 30 m.

6 Distribution of events in time and amplitude

Figure 7 presents the time series of the signal peak amplitudes for all of the multiplets, except multiplet R, which occurred in November. Figure 8 highlights the characteristics of the basal events between March 31 and April 12. The distribution of the events in time is relatively complex. At long time scales, the events of each multiplet are clustered into one or more bursts of events. These active periods last for several hours or days, and they are separated by quiet periods that last for several days. Within each active period, events occur quasi periodically in time.

For intermediate time scales, the distribution of the interevent times show peaks at characteristic times, from several minutes to hours (Figure 9b). Considering the multiplets with at least 100 events, this characteristic time varies from 7 min for multiplet J to 7 h for multiplet M.

For times shorter than 1 s, and only for multiplets B and E, there is another strong peak in the distribution of the interevent times. Figure 10a shows the distribution of the interevent times for small ($A < 160\ \mu m/s^2$) and large ($A > 160\ \mu m/s^2$) events of multiplet B. For these small events, the distribution of the interevent times in the time interval from 0.1 s to 100 s can be fitted by a power

law with an exponent of ≈ 1. Inter-event times as short as 0.01 s have been detected. Such doublets are difficult to detect, as the waveforms of the two events are mixed together. Therefore, the cut-off of the distribution at times shorter than 0.1 s is likely to be due to catalog incompleteness. For longer interevent times, the distribution for small events is similar to that of larger events, and shows a narrow peak at 10 min.

The quasi-periodic behavior of basal icequakes underneath Glacier d'Argentière is similar to observations in Antarctica [*Smith*(2006), *Wiens et al.*(2008), *Zoet et al.*(2012)], although our events are not as regular in time and amplitude. Our observations are more similar to the icequakes detected at Mount Rainier, a temperate mountain glacier [*Thelen et al.*(2013), *Allstadt and Malone*(2014)]. These studies also reported gradual changes in amplitude and interevent time. [*Allstadt and Malone*(2014)] suggested that icequakes detected at Mount Rainier are triggered by changes in subglacial hydrology in response to snow loading. They observed a clear peak of the cross-correlation between precipitation and the rate of seismic activity. We applied the same analysis to our data here, but we found no correlation between the rate of basal icequakes and precipitation. The great sensitivity of the icequake activity at Mount Rainier to snow loading is probably because these events are mostly located on steep hanging glaciers [*Allstadt and Malone*(2014)].

[*Vivian and Bocquet*(1973)] also observed temporal variations of the sliding velocity of Glacier d'Argentière, with a succession of stick phases and periods of acceleration on time scales of hours or days. The sliding velocity was measured in the tunnels underneath the glacier, near Lognan icefall, about 600 m downstream from sensor S_0 (Figure 1, "cavitometer"). These fluctuations might explain the variability of the basal icequake activity with time, although the velocity below the icefall might not be representative of the velocity further upstream. Indeed, we found no correlation between the rate of basal icequakes and the basal glacier motion.

We found no diurnal variations in the rate of basal events. In contrast, [*Walter et al.*(2008)] reported a strong increase in basal activity at night, which might be explained by extensional ice fracturing caused by the glacier recoupling to its bedrock. These discrepancies further suggest that the mechanisms responsible for basal icequakes at Glacier d'Argentière and Gornergletscher are different.

At short time scales, the distribution of the interevent times is very similar to that observed for repeating earthquakes at Parkfield, a creeping segment of the San Andreas fault [*Nadeau, et al.*(1995), *Lengliné and Marsan*(2009)]. This similarity suggests that the processes that produce these events are also similar; i.e., repeated rupture of an asperity or "sticky spot" that is loaded by stable slip around the asperity (i.e., glacier motion for icequakes, and aseismic slip on the fault for earthquakes).

Looking at all of the events within each multiplet, we found only a very weak positive correlation between the interevent times and the peak amplitudes, as illustrated in Figure 11 for multiplet B. Although the fit is poor ($R^2 = 0.09$), the probability of finding such a correlation by chance for 766 independent events is less than 10^{-16}, and thus this correlation is highly significant. This correlation is only visible at times shorter than about 25 min, and for some multiplets. Selecting only the interevent times in the range of 1 min to 30 min, we found a significant correlation at the 95% confidence level for 8 multiplets out of 18. A positive correlation between the amplitude and the interevent times was also found for icequakes observed at Mount Rainier [*Thelen et al.*(2013), *Allstadt and Malone*(2014)] and in Antarctica [*Zoet et al.*(2012)], and for repeating earthquakes along the Calaveras fault in California [*Vidale et al.*(1994)], although with a much clearer correlation. A correlation between the interevent times and the amplitude should be observed if the basal icequakes are associated with glacier motion on an asperity, and if all of the slip on this asperity was accommodated by basal icequakes. The longer the time since the last event, the stronger the next event should be to accommodate the accumulated stress, as long as viscous relaxation is not important. As the correlation is very weak, this might

suggest that basal icequakes only release a small fraction of the basal slip, because the glacier is sliding aseismically between events, or the glacier sliding velocity fluctuates in time or space.

We looked for interactions between the multiplets on time scales of several minutes, as observed for repeating earthquakes in California [*Nadeau, et al.*(1995)]. We estimated the rate of basal icequakes for each multiplet as a function of the time since the last event of another multiplet, for times from 0.1 s to 1 h. However, we found no increase in the rate of basal events, which suggests that there is no triggering between different multiplets.

The distribution of peak amplitudes often shows several distinct peaks, as shown in Figure 9b for all of the multiplets with more than 100 events. This distribution is relatively narrow compared with shallow or intermediate-depth icequakes [*Helmstetter et al.*(2014)], which show a power law distribution of peak amplitudes. The cut-off for amplitudes $\approx 100\ \mu m/s^2$ is likely to be due to catalog incompleteness for small amplitudes.

7 Source migration over time?

Assuming that the source lies on a fixed asperity of the bedrock, there should be slow variation of the source-sensor distance d with time, because the sensor moves with the glacier at a velocity of about 18 cm/d [*Ponton et al.*(2014)]. To test this hypothesis, for all of the multiplets, we analyzed how this distance evolves with time. We can estimate more precisely the time delay between the P-waves and S-waves, so the distance d given by Equation (1), by fitting each signal of a given multiplet to the following signal:

$$y_t(t) = y_{t,P}(t - \Delta t_P) + y_{t,S}(t - \Delta t_S) \tag{3}$$

where $y_{t,P}$ and $y_{t,S}$ are the parts of the template signal that correspond to the P-waves and S-waves, respectively, and Δt_P and Δt_S are the time delays. For each signal, we searched for the values of Δt_P and Δt_S that maximize the correlation between this signal and the template event y_t. The inversion starts with a grid search, then the best values of Δt_P and Δt_S are chosen as the starting values of a simplex optimization.

We found significant variations in the time delay between the P-waves and S-waves for some of the longest and largest multiplets. Figure 12 shows the temporal variation of the time delay between the P-waves and S waves (proportional to the source-sensor distance) for a selection of multiplets that showed at least 90 events and that were active prior to April 12. We do not show the results for multiplets E and H, because we found no significant changes in $t_S - t_P$ for these multiplets. We applied linear regression to each time series between February 22 and April 12 (Figure 12, solid lines) and found that the maximum change in $t_S - t_P$ estimated from the fits is 0.6 ms. If the seismic wave velocities were constant, this corresponds to a change in source-sensor distance of about 2 m in about 1 month. For multiplet B, we obtain an average change in d of 3.79 ± 0.08 cm/d (one standard error) between February 22 and April 12. The events that occurred before and after the gap, so between February 25 and April 2, might rupture a different asperity. Therefore, we also selected only the events that occurred between April 2 and April 12, and measured a variation of 2.66 ± 0.50 cm/d, which is consistent with the slope estimated before. Assuming that these variations of d are due to movement in the flow direction, the displacement is much larger than the change in source-sensor distance d. This corresponds to a displacement equal to $3.79/\sin(\phi_c)/\cos(\alpha - \alpha_g) = 13$ cm/d, where $\alpha_g = 305$ degrees N is the glacier flow direction. Considering the uncertainties on the slope of the linear regression and on the azimuth and incidence angles, and a 5 degrees uncertainty in the glacier flow direction, the 95% confidence interval is from 9 cm/d to 26 cm/d. The observed changes in $t_P - t_S$ are thus consistent

with displacement of the sensor with the glacier at a velocity of 17 cm/d (measured by GPS SERA in winter, and in the central part of the glacier [*Ponton et al.*(2014)]).

However, the variations of $t_S - t_P$ are not always consistent with the estimated source locations and the assumption of a fixed source. For most multiplets, we found a decrease in $t_S - t_P$ with time, even though some sources are located upstream from the sensor (B, J), so that d should increase if the source was fixed, and another one downstream (D).

Moreover, we also found large variations of $t_S - t_P$ for April 10-12, especially for multiplet G, as shown in Figure 13c. Between the first event of this multiplet on March 31 and April 9, there is little variation of $t_S - t_P$ (Figure 12). Then $t_S - t_P$ decreases by 0.4 ms on 1 day and increases by 0.3 ms on the next day. A similar variation of $t_S - t_P$ is also observed at the same time for multiplets B and J, but with smaller amplitudes and with more scatter. The successive decrease and increase in $t_S - t_P$ for multiplets G and B is associated with a similar evolution of peak amplitude A and correlation C. It also comes with a progressive change in the seismic waveforms, as illustrated in Figure 14. The amplitudes of the P-waves on the horizontal traces increase after April 10. The amplitudes and arrival times of late S-wave arrivals also evolve with time after April 9.

The change of 0.4 ms in $t_S - t_P$ for multiplet G corresponds to a change in source-sensor distance of 1.2 m, assuming constant seismic-wave velocities. Considering the uncertainties on the incidence angles ($\phi_c = 1 \pm 5$ degrees), this corresponds to a displacement along the flow direction of at least 14 m (in absolute values), which is about 80 times the average daily displacement of the glacier. This value is therefore too large to be due to glacier motion.

Assuming that this variation of d is instead due to vertical displacement of the glacier in response to horizontal strain or to glacier bedrock separation, the estimated vertical displacement of 1.2 m is still 10 times greater than the displacements observed during 'spring events' [*Anderson et al.*(2004), *Ponton et al.*(2014)]. The observed apparent variations of $t_S - t_P$ for April 10-12 are thus too large to be explained by either glacier flow or vertical displacement.

Another hypothesis is that these apparent variations of $t_S - t_P$ reflect temporal changes in seismic-wave velocities. A variation of the time delay between the P-waves and S waves of 0.4 ms can be explained by a decrease in the shear-wave velocity of only 0.3%. Such a change might result from a change in the water content within crevasses, or from the opening of fractures. However, there was no liquid precipitation during that time (only snow melt for April 10-11). Moreover, we observed no increase in the rate of shallow or intermediate-depth events, or in the basal sliding velocity measured by the cavitometer, from April 9 to April 12 [*Helmstetter et al.*(2014)].

[*Allstadt and Malone*(2014)] also looked for migration of seismic sources at Mount Rainier, although using a different approach and different assumptions. They assumed that the sensor was fixed (outside of the glacier) but that the source was located on dirty patches of basal ice, and was hence moving with the glacier at $\approx$ 1 m/d. As their signals were low-frequency and lacked clear P-wave and S-wave arrivals, they used coda-wave interferometry to measure temporal changes in the source-sensor distance. This method provided the absolute change in source-sensor distance, but not the direction of the motion. They concluded that the apparent migration of the seismic sources was consistent with glacier motion, although it was a little faster than expected.

8 Seismic waveform modeling

Synthetic seismograms were generated using the discrete wavenumber methods [*Bouchon and Aki*(1977)] and they were compared with the observed signals. We assumed a

flat-layered medium with an ice layer over the bedrock. The ice thickness was fixed equal to the estimated depth of each multiplet, between 129 m and 204 m. The rupture is modeled by a point-source. We compared the results obtained for a horizontal tensile fault opening (i.e., the mechanism of basal icequakes suggested by [*Walter et al.*(2010)]) and for shear displacement (double couple) parallel to the glacier flow direction. The fault plane is horizontal with a strike of 35 degrees N, perpendicular to flow direction. For the ice and the granitic bedrock, the P-wave velocities were fixed to 3610 m/s and 5000 m/s, respectively, and the S-wave velocities to 1610 m/s and 2550 m/s, respectively. Following [*Walter et al.*(2009), *Walter et al.*(2010)], the rupture velocity was fixed to $V_R = 1500$ m/s, and the density was fixed to 900 kg/m^3 in the ice and 2750 kg/m^3 in the bedrock.

The frequency content of the simulated signals is controlled both by the rise-time τ (duration of slip) and by the attenuation factor Q. We tested different values of τ and Q to reproduce the frequency content of the data. We first assumed that the attenuation factors are equal to $Q_P = 600$ and $Q_S = 300$, as in [*Walter et al.*(2009), *Walter et al.*(2010)]. But we found that these values do not fit well the frequency content of the data and the relative amplitude of P and S waves. Figure 15 compares real and synthetic seismograms for multiplets B and O assuming shear faulting and using different values of Q and τ. The red lines correspond to low attenuation ($Q_P = 600$ and $Q_S = 300$) and $\tau = 5$ ms. This model underestimates the amplitude of P waves. In addition, the dominant frequency of the simulated signal is too low for P waves but too high for S waves. We thus tested other values for the attenuation factor. Several studies have suggested much lower values of Q, especially for temperate ice [*Peters et al.*(2012), *Mikesell et al.*(2012)]. We generated synthetic seismograms for larger attenuation $Q_P = Q_S = 20$. Increasing the attenuation (i.e., decreasing Q) tends to decrease the frequency content. Therefore, we also decreased the risetime from $\tau = 5$ ms down to $\tau = 1$ ms, to match the duration of the S pulse. The seismograms for this second model are shown as the blue lines in Figure 15 and better explain both the amplitude and the frequency content of P and S waves.

Numerical tests for different values of Q and τ suggest that $\tau = 5$ ms is a maximum upper bound. Larger values of τ cannot explain the frequency content of the data. But we cannot estimate a minimum bound for τ, because for large attenuation ($Q \approx 20$) the frequency content becomes independent of the risetime when $\tau \leq 1$ ms. In Figure 15, the frequency content of the S-waves is similar for both of the models, even if τ varies by a factor of five.

For multiplet B, as for most of the other multiplets, the model provides a relatively good fit to the data, considering the simplicity of the model, the uncertainties on the source locations and focal mechanisms, and the under-sampling. The root-mean-square error, divided by the standard deviation of the data, is 0.28 for the first model (high Q) and 0.16 for the second model (low Q). For multiplet O however, the seismograms are very different for observed and synthetic seismograms, which suggests that this multiplet has a different fault mechanism. The signals for multiplet O cannot be explained by a tensile crack model as suggested by [*Walter et al.*(2010), *Walter et al.*(2013)]. This model would produce P waves either positive (opening crack) or negative (closing crack) in the direction of propagation, and in both cases the tensile crack model does not explain the observed polarity of P waves in the three directions.

We then tested wether the seismic waveforms for all multiplets are better modeled by a tensile failure or by a shear failure parallel to the glacier flow direction. We did not try to fit the seismograms but simply compared the peak amplitudes of P and S waves in the data and in the two fault models. Synthetic seismograms were simulated using $\tau = 1$ ms and $Q_P = Q_S = 20$. We estimated the peak amplitude of the P-waves and S-waves for the three components, using a time window of 0.01 s after the theoretical arrival time of the direct P-waves and S-waves. The same method was also used to estimate the peak amplitude of the observed seismograms. The template seismograms in acceleration

were integrated to obtain the ground velocity. Both the observed and simulated seismograms were band-pass filtered between 30 and 500 Hz. The results are shown in Figure 16. The shear fault model better explains the observed amplitudes of the P-waves and S-waves than a tensile fault. We first consider only the sign of the peak amplitudes, which provides important information on the rupture mechanism. The shear fault explains $80/108 = 74\%$ of the observations, compared with 48% for the tensile-fault model. This success ratio of 74% is very unlikely to be due to random chance (probability of 3×10^{-7}, given by the binomial distribution). The shear fault model explains the variability of the vertical P-wave polarity and that for most multiplets the polarity of the horizontal S-waves is positive for the north component and negative for the east component; i.e., positive in the direction of the slip. In contrast, the tensile fault models predicts a positive polarity of vertical P-waves for all multiplets, and greatly overestimates the amplitude of the vertical P waves in most cases. The results for the P-waves arise arguable for some multiplets because of the difficulty in picking the P-wave first arrivals (see Figure 2). In contrast, the arrival times of the S-waves and their amplitudes are clearly defined for all of the multiplets. We also computed the root-mean-square error (normalized by the standard deviation of the data) between the observed and simulated amplitudes. We found an error of 0.76 for the shear fault model and 1.38 for the tensile fault, showing that the shear fault model better explains both the polarities and the amplitudes of P and S waves.

The source length L can be roughly estimated from the risetime τ and the rupture velocity V_R by $L = \tau\ V_R$. A risetime of 5 ms thus corresponds to a rupture length $L \approx 7.5$ m, and $\tau = 1$ ms corresponds to $L = 1.5$ m. Because we only have an upper bound for the risetime $\tau \leq 5$ ms, this implies that we cannot estimate the rupture length from the seismograms. We can only determine an upper bound $L_{\max} \approx 7.5$ m. Some studies have proposed a smaller rupture velocity for basal icequakes in Antarctica, as down to $V_R = 400$ m/s [*Wiens et al.*(2008)]. Decreasing V_R would decrease the estimated rupture length.

We also estimated the range of the seismic moment that would be needed to explain the variability of the recorded peak amplitude. We assume a fixed risetime $\tau = 1$ ms and attenuations factors $Q_P = Q_S = 20$ and vary the seismic moment to fit the amplitude of the seismograms. The seismic moment M_0 of all basal icequakes ranges from 2×10^4 to 6×10^5 N.m. The seismic moment magnitude, which is estimated by $M_w = 2/3 \log_{10} M_0 - 6.03$ [*Hanks and Kanamori*(1979)], ranges from -3.2 to -2.2. These values are smaller than those reported in previous studies, with moment magnitude varying between $M_w = -0.8$ for basal icequakes at Gornergletscher [*Walter et al.*(2010)], $M_w =$ between -1 and 0 at Mount Rainier [*Thelen et al.*(2013)] and $M_w = 1.8$ in Antarctica [*Zoet et al.*(2012)].

The seismic moment is defined as $M_0 = \mu S \delta$, where $\mu = \rho V_S^2 = 2.3$ GPa is the shear modulus of ice, $S \approx L^2$ is the rupture area, and δ is the slip. Because we can only estimate an upper bound for the rupture length, we can only determine a lower bound for the seismic slip from the estimated seismic moment. For the largest event with $M_0 = 6 \times 10^5$ N.m and assuming $L \leq 7.5$ m, we obtain $\delta \geq 1.5$ μm. Assuming $L = 0.3$ m, similar to the size of large rock debris within the ice [*Vivian and Bocquet*(1973)], we obtain $\delta = 3$ mm.

An upper bound for the seismic slip can also be obtained from the basal shear stress. The ratio of seismic slip and rupture length is related to the stress drop $\Delta\tau$ by

$$\frac{\delta}{L} = \frac{7\pi}{16} \frac{\Delta\tau}{\mu} \tag{4}$$

for a circular rupture of radius L [*Eshelby*(1957)]. The stress drop cannot exceed the shear stress underneath the glacier. The normal stress can be estimated by $\sigma_n = \rho g H$, where $H = 190$ m is the ice thickness, $g = 9.8\ m/s^2$ the acceleration constant, yielding $\sigma_n = 1.7$ MPa. The friction coefficient of

ice on rock measured during laboratory experiments does not exceed 0.6 [*Zoet et al.*(2013)], yielding a maximum shear stress and a maximum stress drop of $\Delta\tau = 1$ MPa. The maximum slip can thus be estimated from the maximum possible rupture length $L_{\max} = 7.5$ m and from the stress drop using the relation (4) yielding $\delta_{\max} = 4.5$ mm. If the slip per event is 3 mm, within the upper range of possible values, and the interevent time is 20 min, then the daily cumulated slip due to icequakes is 22 cm, which is similar to the glacier motion. [*Zoet et al.*(2012)] obtained similar values of seismic slip (0.1-2.6 mm) as in our study despite larger moment magnitudes $M_w = 1.8$ and much longer ruptures (175-1200 m). They also concluded that seismic slip may locally accommodate all of the basal motion of the glacier.

In our data, we observed no change in the seismic waveforms within each multiplet despite variations of peak amplitudes as large as a factor of 18. There are two ways to explain these observations. Either the rupture length is constant for all events, and variations of peak amplitude are due to variations of slip by up to a factor 18, therefore stress drop also varies by a factor 18. Or the stress drop is constant, as is generally observed for earthquakes [*Kanamori and Brodsky*(2004)], and both the rupture length and the slip increase for the largest events. Because of the large attenuation, we cannot detect changes in rise-time or in rupture length as long the rupture length is smaller than about 10 m.

[*Lengliné et al.*(2014)] also reported observations of earthquakes with similar frequency content but very different magnitudes, for a multiplet of repeating earthquakes that occurred during a water circulation test in a geothermal reservoir. This suggests that all events within the multiplet have the same rupture length but varying seismic slip and stress drop, by as much as a factor of 300. [*Lengliné et al.*(2014)] assumed that these variations reflect a transition from stable to unstable slip on the imaged asperities, caused by changes of fluid pressure. The same mechanism may also explain our observations. We suggest that temporal changes in peak amplitude within each multiplet are due to variations in the coupling, with small amplitudes corresponding to a large fraction of aseismic slip on the asperity.

These numerical simulations were also used to test the polarization analysis and the correction for free surface effects (2). The accuracy measured by the median of the absolute error is of 1 degrees for the azimuth and 4 degrees for the incidence angle. The error can, however, be much larger near the nodal planes, where the amplitude of the P-waves is zero.

9 Conclusions

We detected icequakes near the ice-bedrock interface at Glacier d'Argentière. We identified 18 multiplets of basal icequakes that had very similar waveforms within each multiplet. Their distribution in time is relatively complex. At long time scales, the activity shows a succession of active and quiet periods that last for several days or for weeks. At intermediate time scales, events occur quasi-periodically in each of the multiplets, with interevent times ranging from a few minutes to several hours. At times scales shorter than 100 s, we observed an additional regime for events of multiplet B that was characterized by a power-law distribution of the interevent times. Compared with intermediate depth events, the distributions of the amplitudes and the interevent times are much narrower [*Helmstetter et al.*(2014)]. Also, we observed temporal variations of event amplitudes as a function of time that were similar to those reported by [*Thelen et al.*(2013)]. However, we found only very weak correlation between the event amplitudes and the interevent times.

We suggest that basal events are due to the stick-slip motion of the glacier. This hypothesis is based on several observations. First, the icequake depths are consistent with the glacier thickness. The wave-

forms are very similar within each multiplet, which suggests an isolated repeating source and similar mechanisms for all of the events within each multiplet. The quasi-periodic behavior is similar to that observed for basal icequakes in Antarctica [*Smith*(2006), *Wiens et al.*(2008), *Zoet et al.*(2012)], which have been clearly associated with stick-slip motion, although our icequakes are not as regular as in Antarctica. At short and intermediate time scales, the temporal distribution of the basal icequakes is similar to that of the repeating earthquakes at Parkfield [*Nadeau, et al.*(1995), *Lengliné and Marsan*(2009)], which have been associated with the shear failure of an asperity surrounded by a creeping fault. Finally, the polarities of the P-waves and S-waves are more consistent with shear faulting on the ice-bedrock interface than with opening or closing of tensile faults. As we observe mixed P-wave polarities (i.e., "up" and "down"), this implies that the source is not pure crack opening or closing. We can thus exclude quarrying as a potential mechanism, because it involves predominantly extensional vertical fractures in the bedrock [*Iverson*(1991)].

We found no diurnal changes in the rate of basal icequakes, unlike the strong diurnal variations of activity described by [*Walter et al.*(2010)] and associated with changes in basal water pressure. This suggests that our basal events are not associated with the opening or closing of tensile faults, as suggested by [*Walter et al.*(2013)].

Basal icequakes are likely associated with the presence of rock debris inside the ice, which can promote stick-slip behavior [*Zoet et al.*(2013)]. The succession of active and quiet phases may be explained by he advection of basal ice with differing debris concentrations over an asperity of the bedrock [*Zoet et al.*(2012)]. The fraction of rock debris might also control the temporal variations of the mean amplitude of the basal events.

The rupture length and slip are difficult to estimate, because the frequency content of the signals is likely controlled by the attenuation rather than by the rupture duration. The seismic slip is estimated in the range from 1 μm up to 4 mm. If the seismic slip is equal to a few millimeters, it is possible that the cumulated seismic slip due to the basal icequakes accounts for all of the glacier motion locally and temporarily. Progressive temporal changes in the peak amplitude of icequakes within each multiplet may reflect a transition between stable and unstable slip on each asperity, as suggested by [*Lengliné et al.*(2014)] for fluid-induced earthquakes.

The seismic waveforms within each multiplet are very similar, but nonetheless, they have significant differences. We observed small temporal variations of the time delay between the P-waves and S-waves, which are difficult to interpret. These variations cannot be explained by displacement of the glacier with time (i.e., the direction of movement is not consistent with the source locations), but they may be induced by small changes in the seismic-wave velocities. [*Allstadt and Malone*(2014)] also observed temporal changes in seismograms, which they interpreted as due to source migration with glacier flow. However, they could not estimate the direction of motion, only the absolute offset, and the observed changes in the coda of seismic signals might also be produced by migration of seismic scatterers. Further studies are needed to understand the origin of these variations, and these might yield important information on the properties of the seismic sources or of the medium. The great similarities of the seismic waveforms within each multiplet can be used to study seismic-source properties (e.g., stress drop, source duration, rupture dimension), as was done by [*Vidale et al.*(1994)] for repeating earthquakes along the Calaveras Fault in California. Changes in seismic waveforms between repeating earthquakes have also been used to infer changes in seismic-wave velocities [*Schaff and Beroza*(2004)]. [*Niu et al.*(2003)] used repeating microearthquakes to detect migration of seismic scatterers, possibly due to stress-induced redistribution of fluids in fluid-filled fractures.

The basal icequakes detected in the present study have relatively low magnitudes in the range of -3.2 to -2.2. Therefore, these might have been been missed in previous studies. Our basal icequakes

also have very high frequency content, and thus require a high enough sampling rate to be detected. [*Roux et al.*(2008)] detected icequakes underneath Glacier d'Argentière using an array located in a subglacial access tunnel behind Lognan icefall. They used a sampling rate of 250 Hz, which was too low to detect P-waves of basal icequakes such as those described in this study, but the S-waves might have been detected. [*Roux et al.*(2008)] claimed that some of the icequakes they detected were associated with basal slip. However, the depth of these events was not constrained in this study. Also, because they detected only S waves, the similarity of seismic waveforms does not imply that all events are closely located.

Finally, further studies would be useful, to confirm these stick-slip events underneath Glacier d'Argentière, and under other Alpine glaciers, to better locate their sources, and to better constrain their source mechanisms. Future studies should use enough sensors to locate the sources and to calculate the focal mechanisms, and have a high enough sampling rate. Coupling seismometers with GPS would also allow thorough analysis for any correlations between microseismic activity and glacier displacement.

Acknowledgments. We thank the Editor, the Associate Editor and two anonymous reviewers for carefully reading the manuscript and providing many constructive suggestions. We thank Fabian Walter, Francesca Raimondi, Olivier Michel, Claudia Röösli, Pierre Dalban, Christian Vincent, Daniel Amorese and Michel Bouchon for interesting discussions. The GLACIOCLIM database is supported by INSU and OSUG, and it provided the meteorological data and bedrock topography. The regional earthquake catalog was provided by Sismalp. We thank Laurent Ott, Olivier Michel, Olivier Harant and others for participating in the installation and maintenance of the seismic network. Some instruments belong to the French National Pool of Portable Seismic Instruments (Sismob-RESIF). This study was supported by PEPS CNRS and by a grant from Labex OSUG@2020 (ANR10 LABX56). P. Comon is supported by the ERC AdG 2013-320594 DECODA. The ISTerre and SigmaPhy team are part of Labex OSUG@2020 (ANR10 LABX56). The seismic data used in this study can be downloaded from `ftp://ftp.osug.fr:/pub/DATA_JGR_ARGENTIERE`.

References

[*Allstadt and Malone*(2014)] Allstadt, K. and S. D. Malone (2014), Swarms of repeating stick-slip icequakes triggered by snow loading at Mount Rainier volcano, *J. Geophys. Res. Earth Surf., 119*, 1180-1203, doi:10.1002/2014JF003086.

[*Anandakrishnan and Bentley*(1993)] Anandakrishnan, S. and Bentley, C. R. (1993), Microearthquakes beneath Ice Streams B and C, West Antarctica: observations and implications, *J. Glaciol., 39*(133), 455-462.

[*Anandakrishnan and Alley*(1994)] Anandakrishnan, S., and R. B. Alley (1994), Ice Stream C, Antarctica, sticky spots detected by microearthquakes monitoring, *Ann. Glaciol., 20,* 183-186.

[*Anderson et al.*(2004)] Anderson, R. S., S. P. Anderson, K. R. MacGregor, E. D. Waddington, S. ONeel, C. A. Riihimaki, and M. G. Loso (2004), Strong feedbacks between hydrology and sliding of a small alpine glacier, *J. Geophys. Res., 109*, F03005, doi:10.1029/2004JF000120.

[*Bindschadler et al.*(2003)] Bindschadler, R. A., King, M. A., Alley, R. B., Anandakrishnan, S. and Padman, L. (2003), Tidally controlled stick-slip discharge of a West Antarctic Ice Stream, *Science, 301*, 1087-1089.

[*Bouchon and Aki*(1977)] Bouchon, M. and K. Aki (1977), Discrete wavenumber representation of seismic source wave fields, *Bull. Seismol. Soc. Am., 67*, 259-277.

[*Caplan-Auerbach and Huggel*(2007)] Caplan-Auerbach, J., and C. Huggel (2007), Precursory seismicity associated with frequent, large ice avalanches on Iliamna volcano, Alaska, USA, *J. Glaciol., 53*(180), 128-140.

[*Carmichael et al.*(2012)] Carmichael, J. D., E. C. Pettit, M. Hoffman, A. Fountain, and B. Hallet (2012), Seismic multiplet response triggered by melt at Blood Falls, Taylor Glacier, Antarctica, *J. Geophys. Res., 117*, F03004, doi:10.1029/2011JF002221.

[*Christianson*(2012)] Christianson, K. (2012), *Geophysical Exploration of Glacier Basal Processes and Grounding Line Dynamics*, PhD thesis, University Park, Pennsylvania State University, 123p.

[*Dalban Canassy et al.*(2013)] Dalban Canassy, P., F. Walter, S. Husen, H. Maurer, J. Faillettaz, D. Farinotti (2013), Investigating dynamics of an Alpine glacier using probabilistic icequake locations (Triftgletscher, Switzerland), *J. Geophys. Res. Earth Surf., 118*, 2003-2018, doi:10.1002/jgrf.20097.

[*Danesi et al.*(2012)] Danesi, S., Bannister, S., and Morelli, A. (2007), Repeating earthquakes from rupture of an asperity under and Antarctic outlet glacier, *Earth Planet. Sci. Lett., 253*, 151-158

[*Deichmann et al.*(2000)] Deichmann, N., Ansorge, J., Scherbaum, F., Aschwanden, A., Bernhardi, F., and Gudmundsson, G. H. (2000), Evidence for deep icequakes in an Alpine glacier, *Ann. Glaciol., 31*(1), 85-90.

[*Eshelby*(1957)] Eshelby, J. D. (1957), The determination of the elastic field of an ellipsoidal inclusion, and related problems, *Proc. R. Soc. A*, 241(1226), 376-396.

[*Fischer and Clarke*(1997)] Fischer, U. H. and G. K. C. Clarke (1997), Stick-slip sliding behaviour at the base of a glacier, *Ann. Glaciol., 24*, 390-396.

[*Gibbons and Ringdal*(2006)] Gibbons, S. J., and F. Ringdal (2006), The detection of low magnitude seismic events using array-based waveform correlation, *Geophys. J. Int., 165* , 149-166.

[*Goodman et al.*(1979)] Goodman, D., G. King, D., Millar, and G. Robin (1979), Pressure-melting effects in basal ice of temperate glaciers: Laboratory studies and field observations under Glacier d'Argentière, *J. Glaciol., 23*, 259-271.

[*Hanks and Kanamori*(1979)] Hanks T. C and H. Kanamori (1979), Moment magnitude scale, *J. Geophys. Res., 84*(B5), 2348-2350.

[*Hantz*(1981)] Hantz, D. (1981), *Dynamique et hydrologie du glacier d'Argentière*, PhD thesis, Univ. of Grenoble, France.

[*Helmstetter and Garambois*(2010)] Helmstetter, A. and S. Garambois (2010), Seismic monitoring of Séchilienne Rockslide (French Alps): analysis of seismic signals and their correlation with rainfalls, *J. Geophys. Res., 115*, F03016, doi:10.1029/2009JF001532

[*Helmstetter et al.*(2014)] Helmstetter, A., L. Moreau, B. Nicolas, P. Comon and M. Gay (2014), Intermediate-depth icequakes and harmonic tremor in an Alpine glacier (glacier d'Argentière, France): evidence for hydrofracturing?, *in press in J. Geophys. Res.*, doi:10.1002/2014JF003288.

[*Ide et al.*(2007)] Ide, S., G. C. Beroza, D. R. Shelly, and T. Uchide (2007), A scaling law for slow earthquakes, *Nature, 447*(7140), 76-79, doi:10.1038/nature05780.

[*Iken et al.*(1983)] Iken, A., H. Röthlisberger, A. Flotron, and W. Haeberli (1983), The uplift of Unteraargletscher at the beginning of the melt season - A consequence of water storage at the bed?, *J. Glaciol., 29*(101), 28-47.

[*Iverson*(1991)] Iverson, N. R. (1991), Potential effects of subglacial water-pressure fluctuations on quarrying, *J. Glaciol., 37*(125), 27-36.

[*Kanamori and Brodsky*(2004)] Kanamori, H., and E. E. Brodsky (2004), The physics of earthquakes, *Reports on Progress in Physics, 67*(8), 1429.

[*Lengliné and Marsan*(2009)] Lengliné, O., and D. Marsan (2009), Inferring the coseismic and postseismic stress changes caused by the 2004, M=6 Parkfield earthquake from variations of recurrence times of microearthquakes, *J. Geophys. Res., 114*, B10303, doi:10.1029/2008JB006118.

[*Lengliné et al.*(2014)] Lengliné, 0., L. Lamourette, L. Vivin, N. Cuenot and J. Schmittbuhl (2014), Fluid-induced earthquakes with variable stress drop, *J. Geophys. Res., 119*, doi:10.1002/2014JB011282

[*Métaxian, et al.*(2003)] Métaxian, J.-P., S. Araujo, M. Mora and P. Lesage (2003), Seismicity related to the glacier of Cotopaxi Volcano, Ecuador, *Geophys. Res. Lett., 30*(9), 1483, doi:10.1029/2002GL016773.

[*Mikesell et al.*(2012)] Mikesell, T. D., K. van Wijk, M. M. Haney, J. H. Bradford, H. P. Marshall, and J. T. Harper (2012), Monitoring glacier surface seismicity in time and space using Rayleigh waves, *J. Geophys. Res., 117*, F02020, doi:10.1029/2011JF002259.

[*Moore, et al.*(2003)] Moore, P. L., J. P. Winberry, N. R. Iverson, K. A. Christianson, S. Anandakrishnan, M. Jackson, M. E. Mathison, and D. Cohen (2013), Glacier slip and seismicity induced by surface melt, *Geology, 41*(12), 1247-1250, doi:10.1130/G34760.1

[*Nadeau, et al.*(1995)] Nadeau, R. M., W. Foxall and T. V. McEvilly (1995), Clustering and periodic recurrence of microearthquakes on the San Andreas Fault at Parkfield, California, *Science, 267*, 503-507.

[*Neave and Savage*(1970)] Neave, K. G. and Savage, J. C. (1970), Icequakes on the Athabasca Glacier, *J. Geophys. Res., 75*(8), 1351-1362.

[*Nettles and Ekstrom*(2010)] Nettles, M., and G. Ekstrom (2010), Glacial earthquakes in Greenland and Antarctica, *Annu. Rev. Earth Planet. Sci., 38*, 467-491.

[*Neuberg and Pointer*(2000)] Neuberg, J. and T. Pointer (2000), Effects of volcano topography on seismic broad-band waveforms, *Geophys. J. Int., 143*, 239-248.

[*Niu et al.*(2003)] Niu, F., P. G. Silver, R. M. Nadeau, and T. V. McEvilly (2003), Stress induced migration of seismic scatterers associated with the 1993 Parkfield aseismic transient event, *Nature, 426*, 544-548, doi:10.1038/ nature02151.

[*O'Neel et al.*(2007)] O'Neel, S., H. Marshall, D. McNamara, and W. Pfeffer (2007), Seismic detection and analysis of icequakes at Columbia Glacier, Alaska, *J. Geophys. Res. 112*, F03S23, doi:10.1029/2006JF000595.

[*Peters et al.*(2012)] Peters, L. E., S. Anandakrishnan, R. B. Alley, and D. E. Voigt (2012), Seismic attenuation in glacial ice: A proxy for englacial temperature, *J. Geophys. Res., 117*, F02008, doi:10.1029/2011JF002201.

[*Pomeroy et al.*(2013)] Pomeroy, J., A. Brisbourne, J. Evans and D. Graham (2013), The search for seismic signatures of movement at the glacier bed in a polythermal valley glacier, *Ann. Glaciol., 54*(64), 149-156, doi:10.3189/2013AoG64A203

[*Ponton et al.*(2014)] Ponton, F., E. Trouvé, M. Gay, A. Walpersdorf, R. Fallourd, J.-M. Nicolas, F. Vernier, and J.-L. Mugnier (2014), Observation of the Argentière glacier flow variability from 2009 to 2011 by TerraSAR-X and GPS displacement measurements, *IEEE Journal of Selected Topics in Applied Earth Observations and Remote Sensing, 7*(8), 3274-3284 doi:10.1109/JSTARS.2014.2349004.

[*Roux et al.*(2008)] Roux, P., D. Marsan, J., Métaxian, G., O'Brien, and L. Moreau (2008), Microseismic activity within a sérac zone in an Alpine glacier (glacier d'Argentière, Mont Blanc, France, *J. Glaciol., 54*(184), 157-168.

[*Schaff and Beroza*(2004)] Schaff, D. P., and G. C. Beroza (2004), Coseismic and postseismic velocity changes measured by repeating earthquakes, *J. Geophys. Res., 109*, B10302, doi:10.1029/2004JB003011.

[*Smith*(2006)] Smith, A. M. (2006), Microearthquakes and subglacial conditions, *Geophys. Res. Lett., 33*, L24501, doi:10.1029/2006GL028207.

[*Stuart et al.*(2005)] Stuart, G., Murray, T., Brisbourne, A., Styles, P., and Toon, S. (2005), Seismic emissions from a surging glacier: Bakaninbreen Svalbard, *Ann. Glaciol., 42*, 151-157.

[*Sugiyama and Gudmundsson*(2004)] Sugiyama, S. and G. H. Gudmundsson (2004), Short-term variations in glacier flow controlled by subglacial water pressure at Lauteraargletscher, Bernese Alps, Switzerland, *J. Glaciol., 50*(170), 353-362.

[*Thelen et al.*(2013)] Thelen, W. A., K. Allstadt, S. De Angelis, S. D. Malone, S. C. Moran, and J. Vidale (2013), Shallow repeating seismic events under an alpine glacier at Mount Rainier, Washington, USA, *J. Glaciol., 59*(214), 345-356, doi:10.3189/2013JoG12J111.

[*Vallon*(1967)] Vallon, M. (1967), *Contribution à l'étude de la Mer de Glace*, Ph.D. thesis, Univ. of Grenoble, France.

[*VanWormer and Berg*(1973)] VanWormer, D., and E. Berg (1973), Seismic evidence for glacier motion, *J. Glaciol., 12*(65), 259-265.

[*Vidale*(1986)] Vidale, J. (1986), Complex polarization analysis of particle motion, *Bull. Seismol. Soc. Am., 76*(5), 1393-1405.

[*Vidale et al.*(1994)] Vidale, J. E., W. L. Ellsworth, A. Cole, and C. Marone (1994), Variations in rupture process with recurrence interval in a repeated small earthquake, *Nature, 368*, 624-626, doi:10.1038/368624a0.

[*Vincent et al.*(2009)] Vincent, C., A. Soruco, D. Six and E. Le Meur (2009), Glacier thickening and decay analysis from 50 years of glaciological observations performed on Glacier d'Argentière, Mont Blanc area, France, *Ann. Glaciol.*, 50, 73-79.

[*Vivian and Bocquet*(1973)] Vivian, R., and G. Bocquet (1973), Subglacial cavitation phenomena under the glacier d'Argentière, Mont Blanc, France, *J. Glaciol., 12*(66), 439-451.

[*Walter et al.*(2008)] Walter, F., Deichmann, N., and Funk, M. (2008), Basal icequakes during changing subglacial water pressures beneath Gornergletscher, Switzerland. *J. Glaciol., 54*(186), 511-521.

[*Walter et al.*(2009)] Walter, F., J. Clinton, N. Deichmann, D. Dreger, S. Minson and M. Funk (2009), Moment tensor inversion of icequakes on Gornergletscher, Switzerland, *Bull. Seismol. Soc. Am., 99*(2A), 852-870.

[*Walter et al.*(2010)] Walter, F., D. Dreger, J. Clinton, N. Deichmann and M. Funk (2010), Evidence for near-horizontal tensile faulting at the base of Gornergletscher, a swiss Alpine glacier, *Bull. Seismol. Soc. Am., 100*(2), 458-472, doi:10.1785/0120090083.

[*Walter et al.*(2013)] Walter, F., P. Dalban Canassy, S. Husen, and J. F. Clinton (2013), Deep icequakes: What happens at the base of Alpine glaciers?, *J. Geophys. Res. Earth Surf., 118*, 1720-1728, doi:10.1002/jgrf.20124.

[*Walter et al.*(2014)] Walter, J., Z. Peng, S. Tulaczyk, and L. H. Beam (2014), Triggering of glacier stick-slip events by distant earthquakes, submitted to *Geophys. Res. Lett.*

[*Weaver and Malone*(1979)] Weaver, C. S. and S. D. Malone (1979), Seismic evidence for discrete glacier motion at the rock-ice interface, *J. Glaciol., 23*(89), 171-183.

[*Wiens et al.*(2008)] Wiens, D. A., Anandakrishnan, S., Winberry, J. P., and King, M. A. (2008), Simultaneous teleseismic and geodetic observations of the stick-slip motion of an Antarctic ice stream, *Nature, 453*, 770-775, doi:10.1038/nature06990.

[*Winberry et al.*(2009)] Winberry, J. P., S. Anandakrishnan, R. B. Alley, R. A. Bindschadler, and M. A. King (2009), Basal mechanics of ice streams: Insights from the stick-slip motion of Whillans Ice Stream, West Antarctica, *J. Geophys. Res., 114*, F01016, doi:10.1029/2008JF001035.

[*Zoet et al.*(2012)] Zoet, L., S. Anandakrishnan, R. Alley, A. Nyblade, and D. Wiens (2012), Motion of an Antarctic glacier by repeated tidally modulated earthquakes, *Nat. Geosci., 5*, 623-626, doi:10.1038/ngeo1555.

[*Zoet et al.*(2013)] Zoet, L. K., B. Carpenter, M. Scuderi, R. B. Alley, S. Anandakrishnan, C. Marone, and M. Jackson (2013), The effects of entrained debris on the basal sliding stability of a glacier, *J. Geophys. Earth Surf., 118*, 656-666, doi:10.1002/jgrf.20052.

multi-plet	N	start date	T days	Δt min	A $\mu m/s^2$	d m	α degrees N	ϕ degrees	ϕ_c degrees	H m
A	250	2012/02/21	24.1	9.5	179	210 ± 8	30 ± 25	26 ± 8	30 ± 11	182 ± 10
B	852	2012/02/22	49.4	12.6	320	224 ± 8	59 ± 13	40 ± 7	49 ± 12 [a]	146 ± 13
C	29	2012/02/23	1.8	22.1	164	207 ± 8	38 ± 43	20 ± 14	23 ± 16	190 ± 14
D	125	2012/03/12	29.0	19.9	402	218 ± 8	328 ± 12	37 ± 7	46 ± 10	152 ± 15
E	197	2012/03/12	5.2	11.9	286	204 ± 8	278 ± 32	17 ± 6	20 ± 8	192 ± 9
F	12	2012/03/13	3.2	393.1	282	259 ± 9	51 ± 3	55 ± 1	[b]	
G	117	2012/03/31	11.5	33.1	1040	201 ± 8	143 ± 57	1 ± 9	1 ± 13	201 ± 8
H	92	2012/04/02	5.4	14.3	192	218 ± 8	67 ± 8	42 ± 5	54 ± 9 [a]	129 ± 17
I	16	2012/04/03	6.2	56.8	205	198 ± 8	280 ± 43	20 ± 5	22 ± 6	183 ± 10
J	182	2012/04/08	3.4	7.2	198	221 ± 8	56 ± 12	32 ± 7	38 ± 9	176 ± 12
K	17	2012/04/26	0.3	19.6	149	192 ± 8	346 ± 20	20 ± 3	23 ± 4	176 ± 9
L	69	2012/04/27	5.0	20.2	428	201 ± 8	323 ± 11	17 ± 2	19 ± 3	190 ± 9
M	254	2012/06/05	13.0	37.9	1021	192 ± 8	118 ± 95	-1 ± 11	-1 ± 13	192 ± 8
N	21	2012/06/09	0.4	13.3	161	195 ± 8	172 ± 73	2 ± 13	3 ± 19	195 ± 8
O	39	2012/06/12	2.4	19.1	1014	213 ± 8	38 ± 14	25 ± 5	29 ± 7	186 ± 11
P	43	2012/06/16	1.5	26.1	315	189 ± 8	310 ± 45	19 ± 10	21 ± 17	177 ± 10
Q	14	2012/06/17	0.5	38.2	1481	207 ± 8	53 ± 29	8 ± 5	9 ± 6	204 ± 9
R	28	2012/11/25	5.3	82.3	374	358 ± 8	134 ± 3	56 ± 4	[b]	

Table 1: **Characteristics of the basal icequakes for each multiplet.** N is the number of events, T is the duration of the multiplet, Δt is the median interevent time, A is the mean peak amplitude, d is the hypocentral distance and H is the source depth. Apparent and corrected incidence angles ϕ and ϕ_c are corrected from the surface slope (the angle is measured relative to the normal of the glacier surface). Uncertainties on α, ϕ and ϕ_c represent the variability of the data within each multiplet (one standard deviation). Location errors on d and H are the 95% confidence intervals, assuming uncertainties in the arrival times and the azimuth and incidence angles. (^{a}): Estimated incidence angle ϕ_c is greater than the critical refraction angle $\phi_r = 46^o$. (^{b}): Estimated incidence angle is greater than the maximum value $\phi^* = 53^o$.

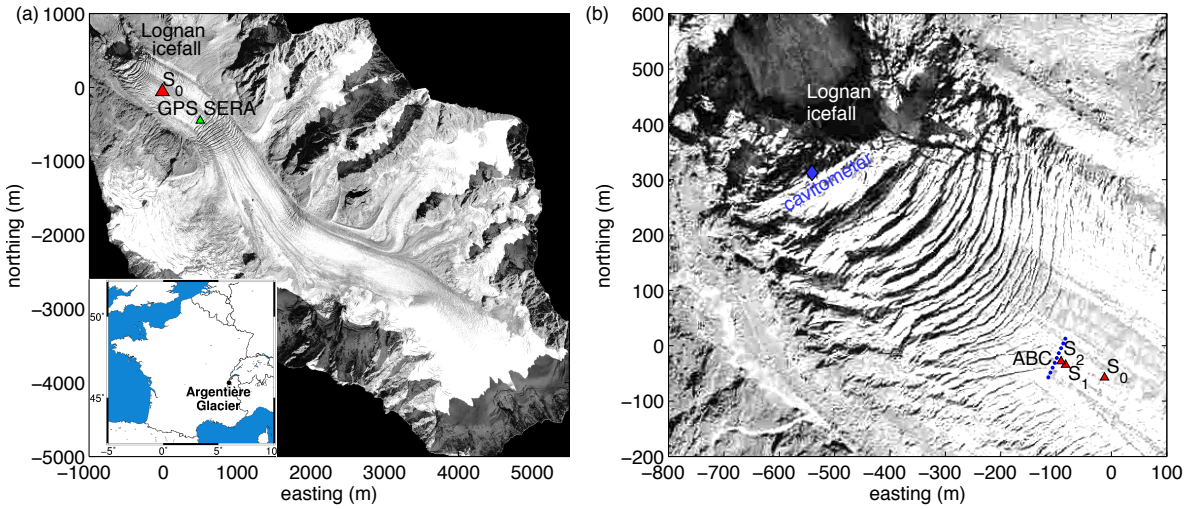

Figure 1: (a) Orthophoto of the glacier taken in 2003 (from GLACIOCIM), and inset showing the location of the glacier in France. Green triangle, location of GPS SERA [*Ponton et al.*(2014)]. (b) Zoom showing the seismic network. Circles (station ABC), velocimeters installed in November 2012; triangles (S_0, S_1, S_2), accelerometers: S_0 was installed in February 2012, and S_1 and S_2 were installed in November 2012. The cavitometer (blue diamond in (b)) is located in a tunnel underneath the glacier and measures the basal slip. The grid origin is 45.964 degrees N and 6.973 degrees E.

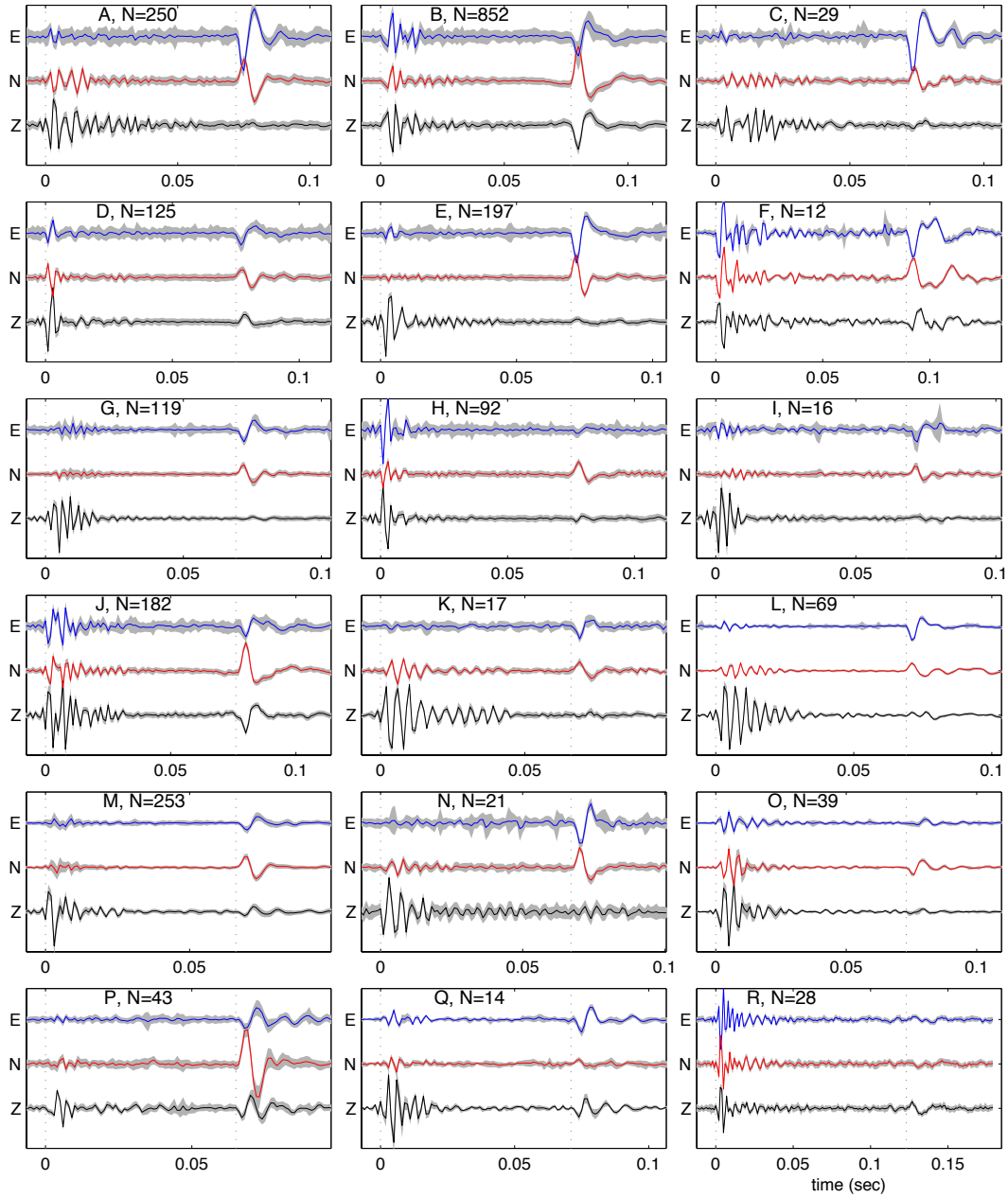

Figure 2: Waveforms of the template events for all of the multiplets (stack of all of the seismograms in ground acceleration normalized by peak amplitude with a 50 Hz zero-phase high-pass filter). Multiplets A, ..., Q were recorded by sensor S_0, and multiplet R by S_1. Dotted lines, arrival times of the P-waves and S-waves; gray patches, variability of the signal for all of the events of each multiplet (one standard deviation of signals normalized by peak amplitude). The number N of events of each multiplet is indicated in each plot.

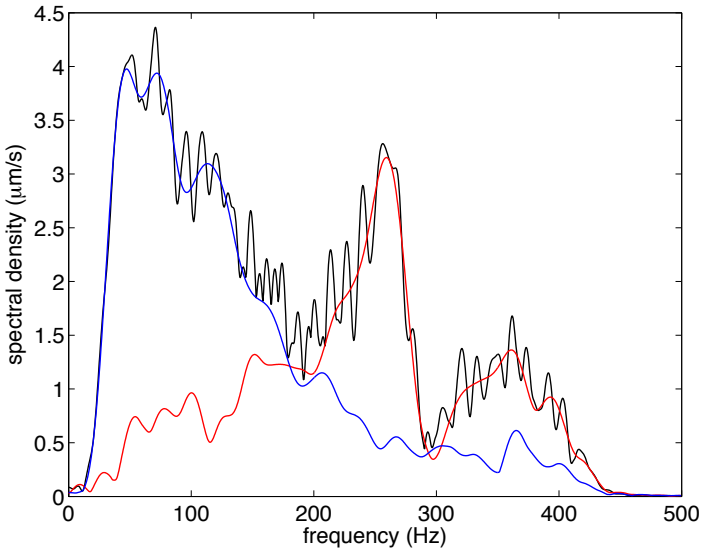

Figure 3: Fourier transform for a basal icequake of multiplet B, averaged over the three components of the signal for the full duration of the event (black line), P-waves (red line) or S-waves (blue line).

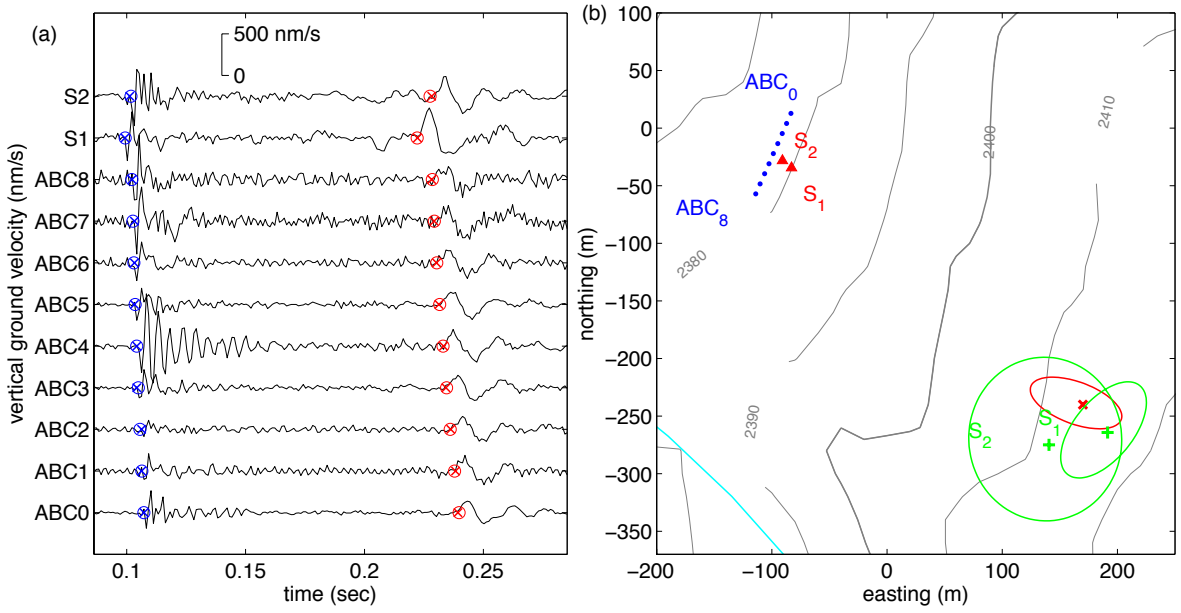

Figure 4: (a) Seismograms for an event of multiplet R recorded by station ABC and by the two accelerometers S_1 and S_2, using a 50 Hz zero-phase high-pass filter. 'x', measured arrival times for the P-waves and S-waves; circles, modeled arrival times. (b) Locations of the seismic sensors (circles, velocimeters; triangles, accelerometers), glacier boundary (blue line) and estimated location of the source using two methods. 'x', location obtained from the P-wave and S-wave arrival times; plus signs, locations obtained from the polarization analysis (see Figure 5) using sensor S_1 or sensor S_2. All of the locations were obtained assuming direct waves. The ellipses show the 95% confidence intervals.

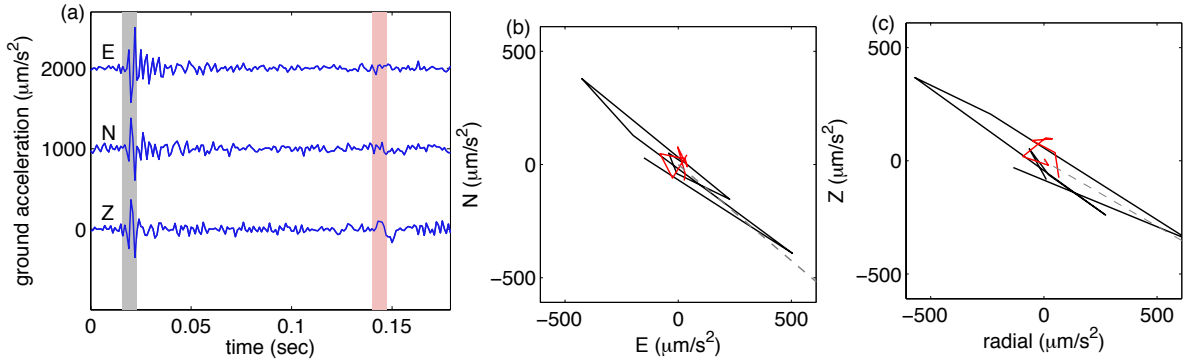

Figure 5: (a) Waveforms of a basal icequake of multiplet R detected by station S_1 (same event as in Figure 4), using a 50 Hz zero-phase high-pass filter. Shaded areas, time intervals of the P-waves and S-waves. The polarization method of [*Vidale*(1986)] provides an estimate of the azimuth $\alpha = 130$ degrees N and of the apparent incidence angle $\phi = 60$ degrees. (b) Particle motion for P-waves (black lines) and S-waves (red lines) in the horizontal plane for the time interval highlighted in (a). (c) Particle motion in the vertical plane parallel to the direction α. Dashed lines, azimuth direction in (b), and incidence angle of P-waves in (c).

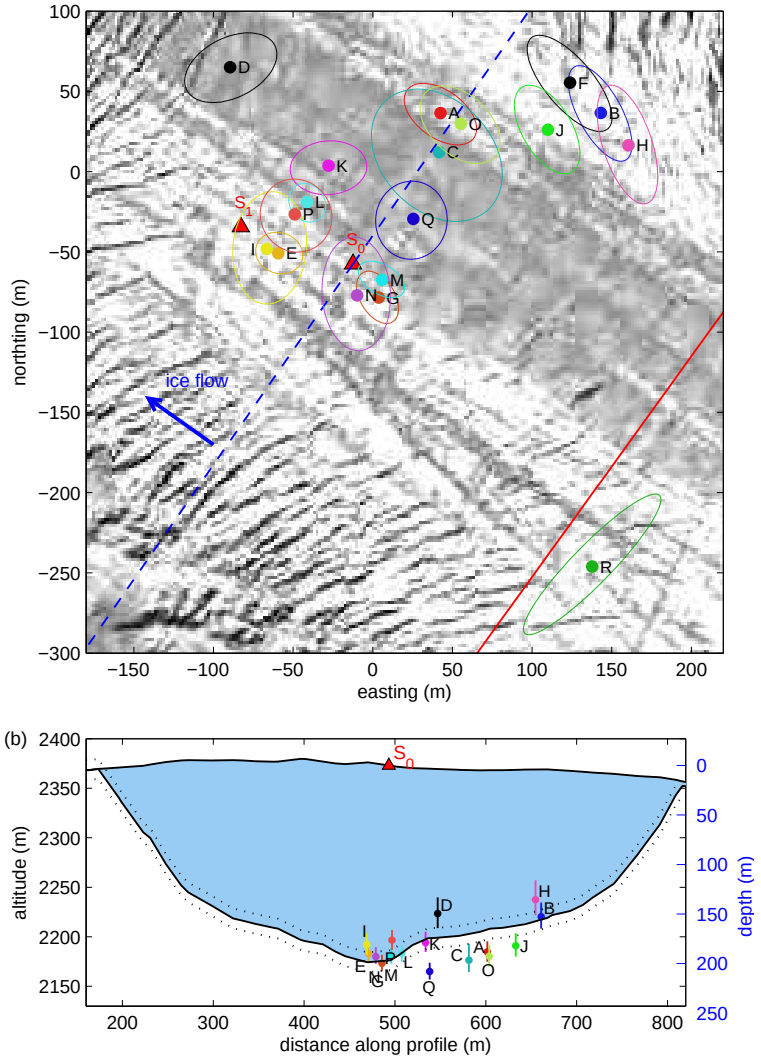

Figure 6: (a) Map of basal icequakes (dots) and error ellipses at the 95% confidence level. Crosses, seismometers (S_0 was operating from February to June 2012, and S_1 in November 2012); dashed blue line, direction perpendicular to the glacier flow. (b) Cross-section along a profile located about 200 m upstream from S_0, and shown as a solid line in (a). The topographies of the bedrock and the surface were obtained from the GLACIOCLIM database [*Vincent et al.*(2009)]. Dotted lines, average uncertainty on the bedrock topography of 10 m [*Hantz*(1981)]. Only multiplets with incidence angles $\phi_c < \phi^*$ are shown, with multiplets F and R rejected.

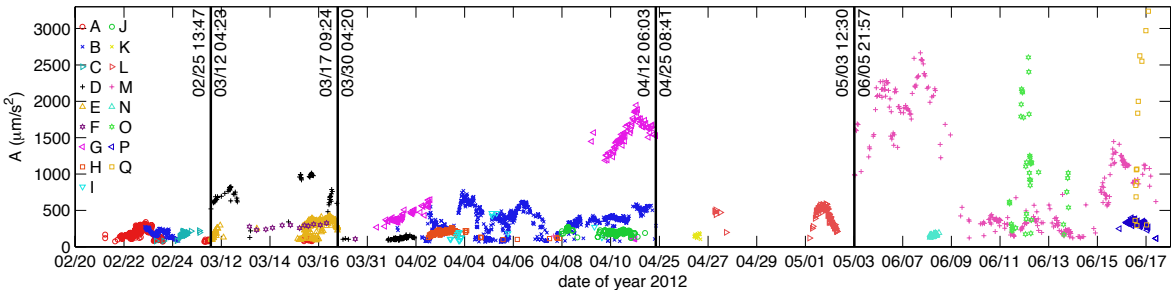

Figure 7: Time series of signal peak amplitudes for all of the multiplets, excluding multiplet R which occurred in November 2012. Note that the time scale is not continuous, gaps are indicated by vertical black lines.

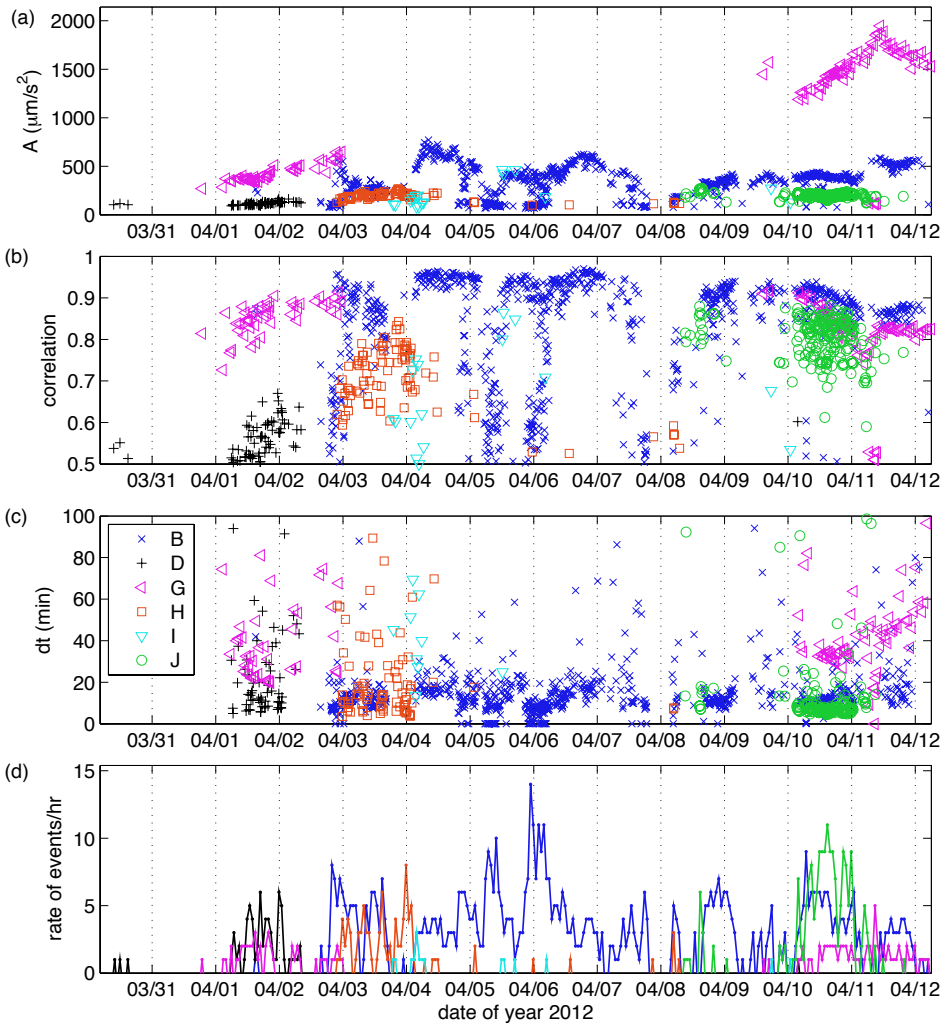

Figure 8: Time series of signal peak amplitudes (a), the waveform correlation (b), the interevent times (c), and the rate of basal events (d), for all of the multiplets active between March 30 and April 12.

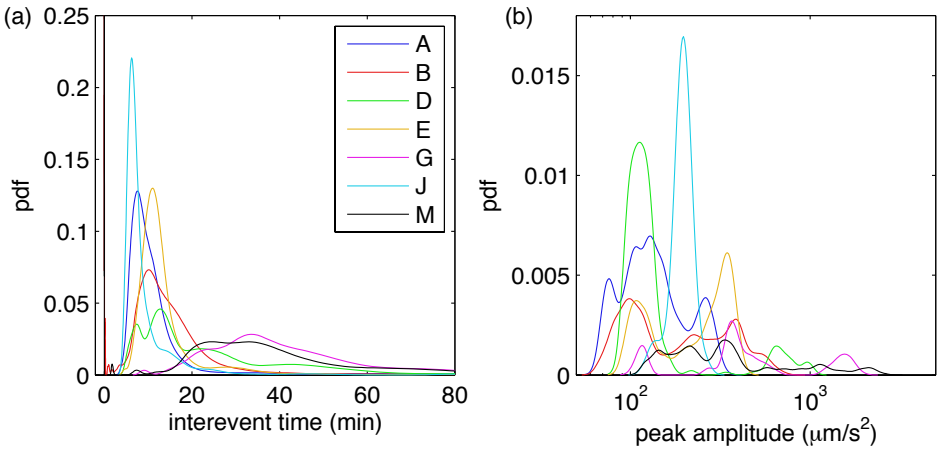

Figure 9: Probability density function of the interevent times (a) and peak amplitudes (b), for all of the multiplets with at least 100 events.

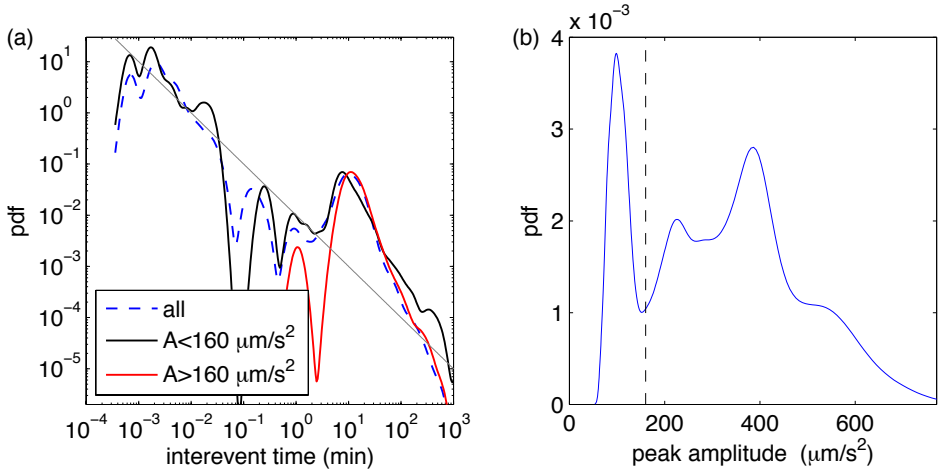

Figure 10: Probability density function of the interevent times (a) and the peak amplitudes (b) for multiplet B. The largest events (peak amplitude $A > 160$ $\mu m/s^2$, value shown by a dashed line in (b)) have a narrow distribution of interevent times peaked at about 600 s. For smaller events, there is an additional power-law regime for short interevent times. Straight line, power-law of exponent -1, for reference.

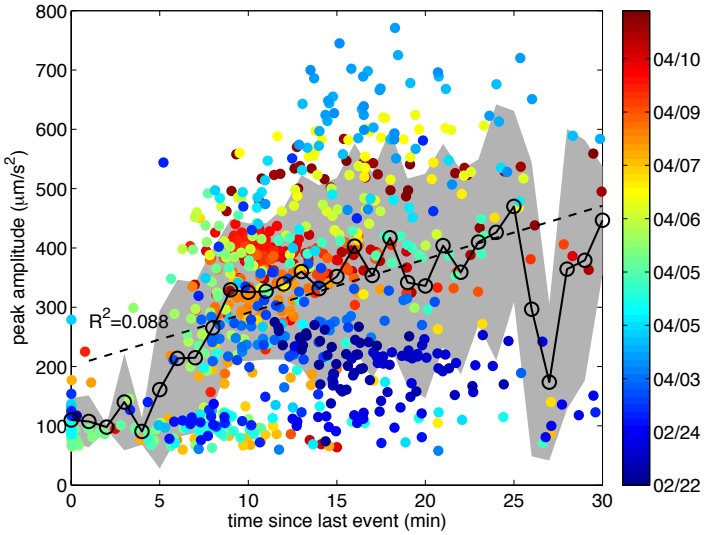

Figure 11: Correlation between peak amplitude and time since the last event for multiplet B. Color scales, event index (first events in blue, last events in red); black dashed line, linear fit for the interevent times from 1 min to 30 min; solid black line, mean peak amplitude for each time bin of 1 min, from 0 min to 30 min. This shows progressive increase in the peak amplitude with the time since the last event. Gray shaded area, standard deviation of the peak amplitude for each time bin.

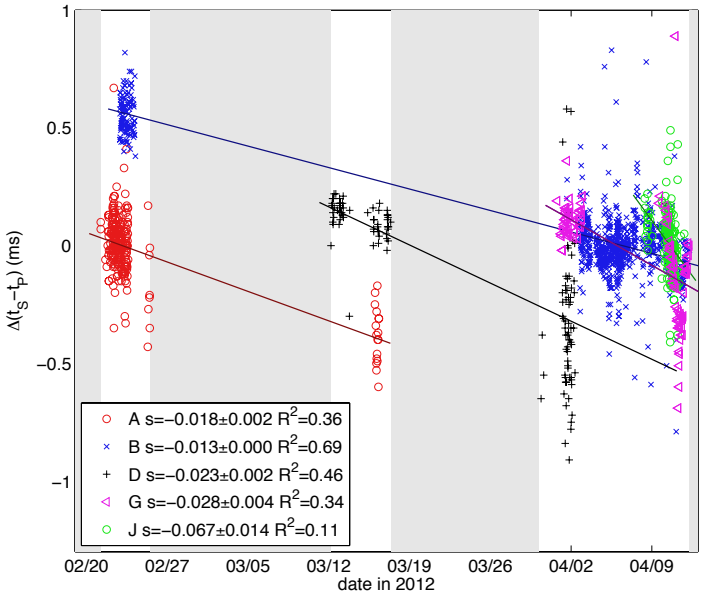

Figure 12: Temporal variations of the time delay between the P-waves and S-waves, relative to the median value within each multiplet. Solid lines, linear regressions. The slope of each fit (in ms/day) and its uncertainty (one standard error), and the correlation coefficient R^2, are shown. Gray shaded areas, when no data were available.

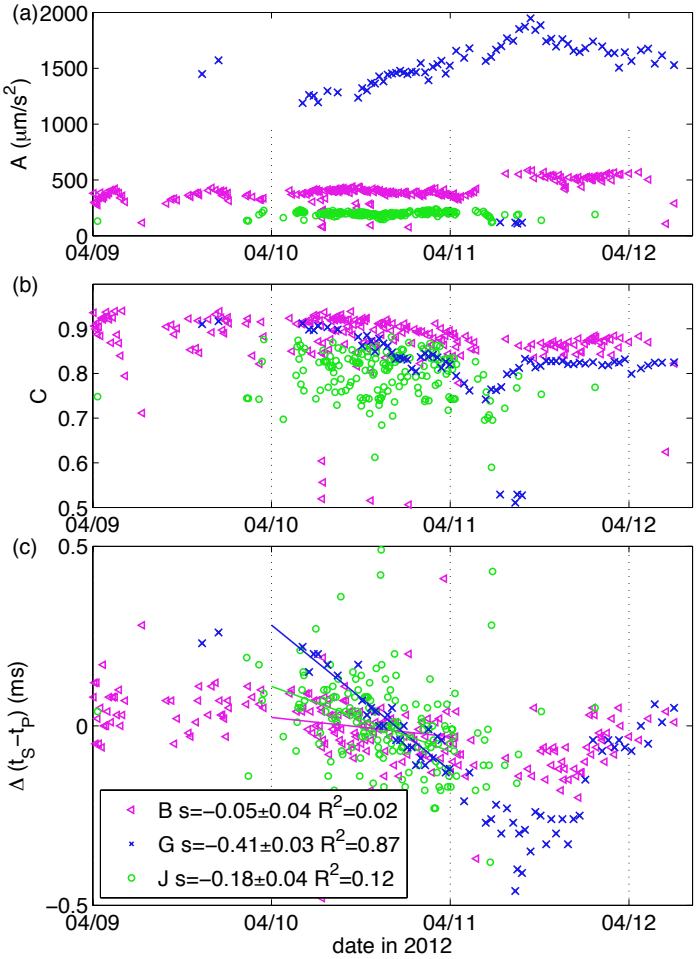

Figure 13: Temporal variations of the peak amplitude A (a), correlation with the template (b), and relative time delay between the P-waves and S-waves (c), for multiplets B, G and J. Solid lines in (c), linear fits for each multiplet using only the events that occurred on April 10. The slope (in ms/day) and its uncertainty (one standard error), and the correlation coefficient R^2, are shown.

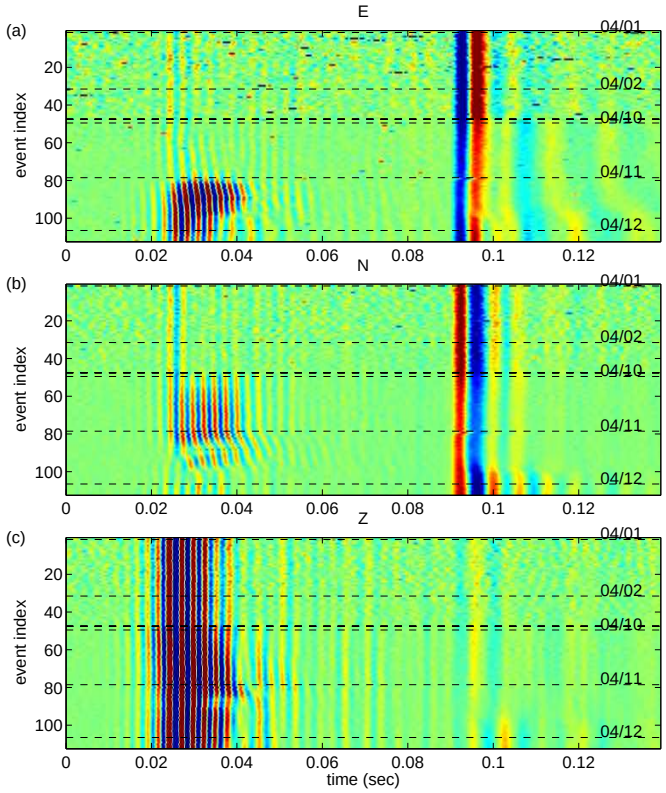

Figure 14: Seismograms for all of the events of multiplet G, normalized by the amplitude, showing the east-west component (a), the north-south component (b), and the vertical component (c). Color scale indicates normalized ground acceleration. Each dashed line indicates a new day.

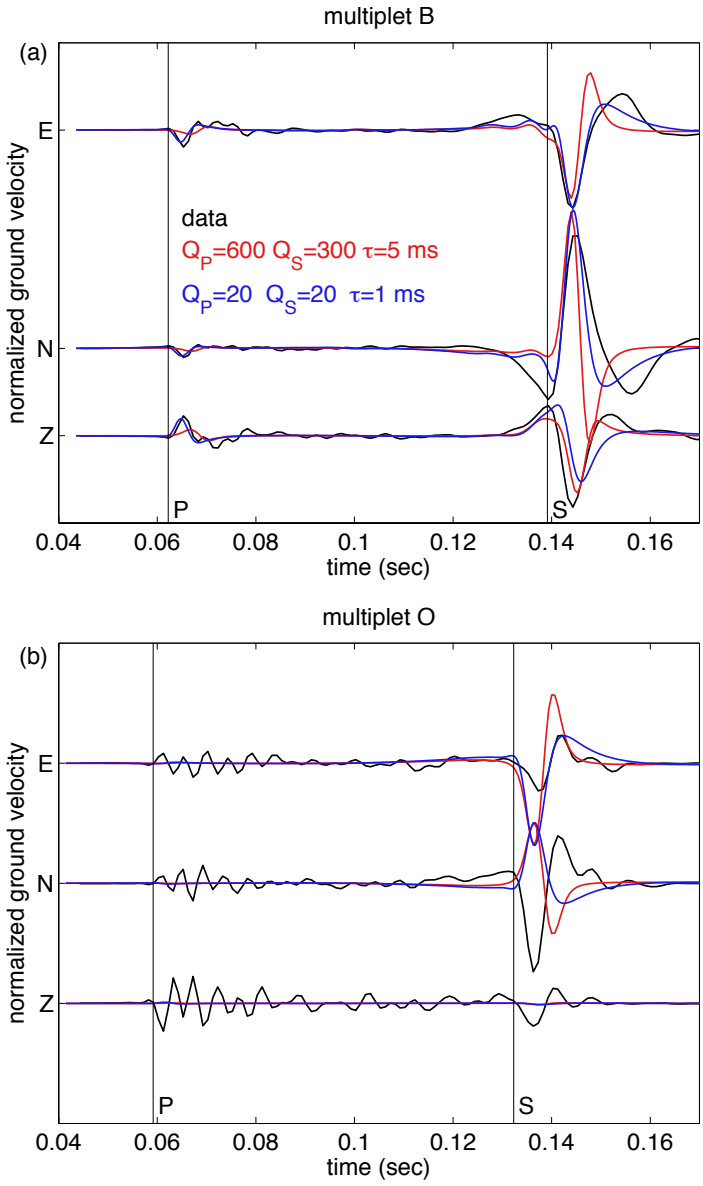

Figure 15: Seismograms (ground velocity bandpass filtered between 30 and 500 Hz) recorded by station S_0 for multiplets B (a) and O (b) (black lines), compared with synthetic signals generated for a horizontal shear fault. The first model (red lines) uses low attenuation $Q_P = 600$, $Q_S = 300$, and a risetime $\tau = 5$ ms. The second model (blue lines) uses high attenuation $Q_P = Q_S = 20$, and a risetime $\tau = 1$ ms. Vertical lines, arrival times of the P-waves and S-waves.

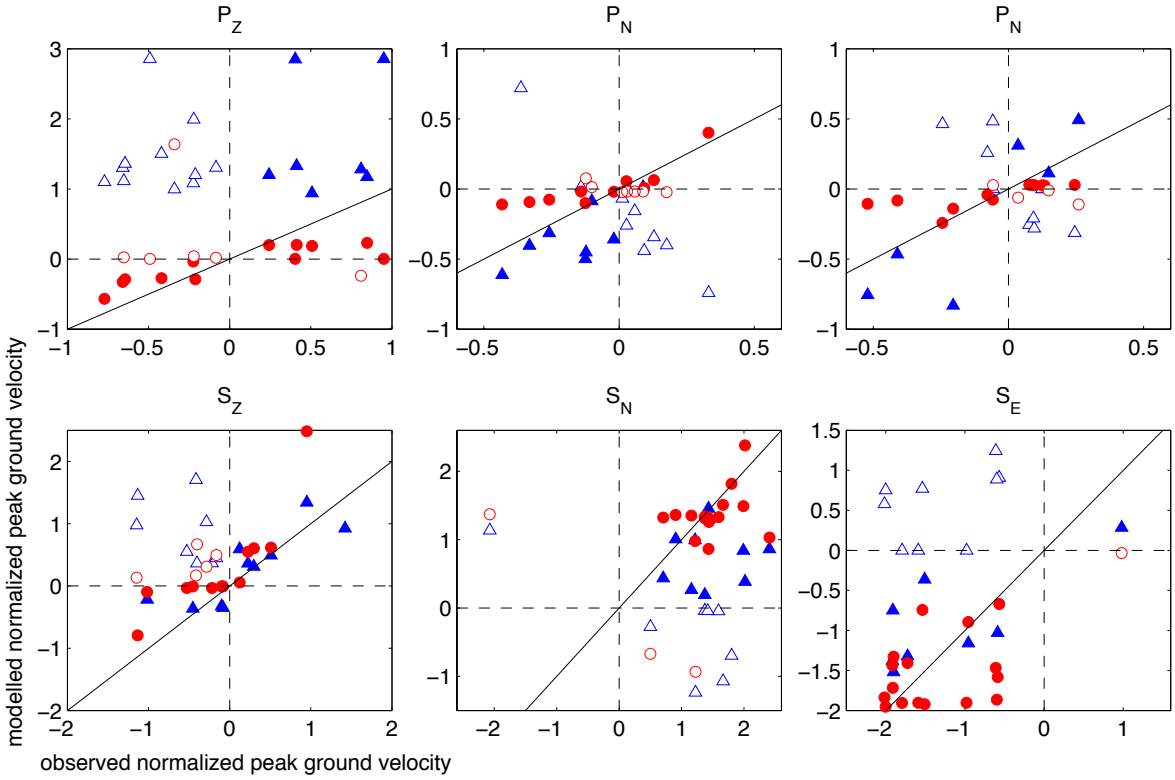

Figure 16: Comparison between observed and simulated peak amplitudes of ground velocity for two models and for the three components ('Z' for vertical, 'N' for North-South and 'E' for East-South displacement) of P waves (top) and S waves (bottom). The first model (blue triangles) assumes tensile failure. The second model (red circles) considers shear slip in the direction of glacier flow. Peak amplitudes of observed and simulated signals have been normalized by the average over the three components of the peak amplitudes in the data. Filled symbols indicate that the modeled polarity (amplitude sign) matches the data. The solid black line represents a perfect fit.